Elsevier Editorial System(tm) for Lithos
Manuscript Draft

Manuscript Number: LITHOS8248R3

Title: Relationships between monazite, apatite and chevkinite-group minerals in the rhyolitic Joe Lott Tuff, Utah, USA

Article Type: Regular Article

Keywords: Joe Lott Tuff; chevkinite-group; monazite; apatite-group; compositional zonation; convective overturn

Corresponding Author: Dr. Boguslaw Baginski, D.Sc.

Corresponding Author's Institution: University of Warsaw

First Author: Joanna Galanciak

Order of Authors: Joanna Galanciak; Boguslaw Baginski, D.Sc.; Ray Macdonald; Harvey E Belkin; Jakub Kotowski; Petras Jokubauskas

Abstract: The high-silica rhyolitic Joe Lott Tuff was erupted at 19.2 ± 0.4 Ma from the Mount Belknap caldera in Utah, USA. Despite having a volume of ca 150 km3 it is compositionally homogeneous and contains ≤3 modal% phenocrysts. The tuff also shows two very unusual aspects of the REE-bearing phases, monazite and the chevkinite-group minerals (CGM): (i) the presence of perrierite-(Ce) in a high-silica rhyolite, and (ii) the replacement of CGM in the stratigraphic sequence by monazite, with a subsequent return to a CGM. Evidence from CGM distribution and variations in monazite and apatite-group composition with stratigraphic height in the deposit are used to infer that prior to eruption the magma was compositionally zoned, the zonation being partially obliterated by convective overturn in the reservoir.

Research Data Related to this Submission

There are no linked research data sets for this submission. The following reason is given:
Data will be made available on request

Revision notes@ LITHOS8248R2

Please find below our responses to the comments by Reviewer 2.

Hydroxylapatite. A sentence has been added to that effect (ll. 257-258).

Table 3. We apologise for this oversight. Table 3 has been amended.

Tables 5 and 6. The abbreviation bd (below detection) and a dash (not determined/analyzed) are in common use, e.g. in our recent Lithos paper (2019, 328-329, 1-13).

Line 39. The space has been added (l.39).

Line 89. We think that the correct number of brackets is there.

We have thanked the reviewers for their help in the Acknowledgements (ll.405-406).

Please let us know if any further amendments are needed.

Relationships between monazite, apatite and chevkinite-group minerals in the rhyolitic Joe Lott Tuff, Utah, USA

ABSTRACT

The high-silica rhyolitic Joe Lott Tuff was erupted at 19.2 ± 0.4 Ma from the Mount Belknap caldera in Utah, USA. Despite having a volume of ca 150 km^3 it is compositionally homogeneous and contains ≤3 modal% phenocrysts. The tuff also shows two very unusual aspects of the REE-bearing phases, monazite and the chevkinite-group minerals (CGM): (i) the presence of perrierite-(Ce) in a high-silica rhyolite, and (ii) the replacement of CGM in the stratigraphic sequence by monazite, with a subsequent return to a CGM. Evidence from CGM distribution and variations in monazite and apatite-group composition with stratigraphic height in the deposit are used to infer that prior to eruption the magma was compositionally zoned, the zonation being partially obliterated by convective overturn in the reservoir.

*Highlights (for review)

Joe Lott Tuff: highlights

- Remarkably homogeneous, crystal-poor, large volume high-silica rhyolitic ignimbrite
- Unique occurrence of chevkinite, perrierite and monazite in same extrusive body
- Pre-eruptive compositional stratification disturbed by convective overturn

Relationships between monazite, apatite and chevkinite-group minerals in the rhyolitic Joe Lott Tuff, Utah, USA

J. Galanciak[a], B. Bagiński[a,*], R. Macdonald[a,b], H. E. Belkin[c], J. Kotowski[a], P. Jokubauskas[a]

[a] Institute of Geochemistry, Mineralogy and Petrology, University of Warsaw, 02-089 Warszawa, Poland

[b] Environment Centre, Lancaster University, Lancaster LA1 4YQ, UK

[c] U.S. Geological Survey retired, 11142 Forest Edge Drive, Reston, VA 20190-4026, USA

° Corresponding author: e-mail B.Baginski1@uw.edu.pl

ABSTRACT

The high-silica rhyolitic Joe Lott Tuff was erupted at 19.2 ± 0.4 Ma from the Mount Belknap caldera in Utah, USA. Despite having a volume of ~150 km^3 it is compositionally homogeneous and contains ≤3 modal% phenocrysts. The tuff also shows two very unusual aspects of the REE-bearing phases, monazite and the chevkinite-group minerals (CGM): (i) the presence of perrierite-(Ce) in a high-silica rhyolite, and (ii) the replacement of CGM in the stratigraphic sequence by monazite, with a subsequent return to a CGM. Evidence from CGM distribution and variations in monazite and apatite-group composition with stratigraphic height in the deposit are used to infer that prior to eruption the magma was compositionally zoned, the zonation being partially obliterated by convective overturn in the reservoir.

KEYWORDS: Joe Lott Tuff; chevkinite-group; monazite; apatite-group; compositional zonation; convective overturn

1. Introduction

The Joe Lott Tuff Member of the Mount Belknap Volcanics is a high-silica rhyolitic ash flow tuff sheet associated with the collapse of the Mount Belknap caldera in west-central Utah at 19.2 ± 0.4 Ma (Fig. 1; Budding et al., 1987; Cunningham and Steven, 1979). The tuff has several unusual petrological features. High-silica rhyolitic eruptions greater than 1 km^3 in size are generally considered to be zoned compositionally and in phenocryst abundance, the zonation being reflected in the nature of the deposits (Hildreth, 1981; Smith, 1979). Despite its size, with a dense rock equivalent (DRE) volume of ~150 km^3, the Joe Lott Tuff is phenocryst-poor (1-3 modal%) and has a very homogeneous composition, e.g. 75.4 to 76.7 wt% SiO_2 (calculated 100%, volatile-free). We are unaware of any other ignimbrite of this volume of such uniformly high-silica composition and phenocryst-poor nature. For example, the Bishop Tuff, California, erupted at 0.7 Ma during formation of the Long Valley caldera, has a DRE volume of 170 km^3, phenocryst abundances ranging from 5 to 25 modal% and SiO_2 in the range ~75 to >77 wt% (Hildreth, 1979). The Devine Canyon Tuff, Oregon, has a minimum volume of 200 km^3 and SiO_2 contents in the range 74.6-77.6 wt%, but has phenocryst abundances ranging from 7 to 30 modal % (Wacaster et al., 2011). The high-silica portion (SiO_2 73-77 wt%) of the Younger Toba Tuff, Indonesia, has a volume >1000 km^3 and contains12-25 wt% phenocrysts (Tierney et al., 2019).

In this study, we report on two further unusual features of the tuff. First, the presence in different units of phenocrysts of chevkinite-(Ce) and perrierite-(Ce), the most common members of the chevkinite-group of minerals (CGM; simplified formula [(REE, $Ca)_4Fe^{2+}(Fe^{2+},Fe^{3+},Ti,Al)_2Ti_2(Si_2O_7)_2$]), although these phases normally form in compositionally different igneous lithologies (Bagiński and Macdonald, 2013; Macdonald and Belkin, 2002; Macdonald et al., 2019a). Second, chevkinite-(Ce) and perrierite-(Ce) phenocrysts are absent from certain units, their place as the main REE-bearing phase being

taken by monazite ($REEPO_4$). So far as we are aware, this is the first record of such a relationship between these phases in an igneous body.

The specific aims are: (i) to document the occurrences and compositions of the CGM and monazite; (ii) to explain the occurrence of perrierite, rather than chevkinite, in a high-silica rhyolite; and (iii) to discuss the factors which controlled the distribution of the minerals. Data for the apatite-group phenocrysts are also included, to determine whether compositional variations in the monazite and CGM are mirrored by those in the apatite.

2. The Joe Lott Tuff

The Joe Lott Tuff Member of the Mount Belknap Volcanics is a composite sheet, changing laterally from a single cooling unit near source to four distinct cooling units distally (Fig. 2). Samples used in this study are all from outflow facies of the tuff. The Lower Unit is up to 64 m thick and has a basal vitrophyre. Initial collapse of the Mount Belknap caldera accompanied eruption of the Lower Unit (Fig. 3). The unit is followed upward by a Middle Unit up to 43 m thick, a 26 m pink-coloured unit, and an Upper Unit 31 m thick (Fig. 3). On the basis of the amount of erosion at the top of cooling units prior to eruption of the next unit, Budding et al. (1987) estimated that the time interval between the Lower and Middle Units was at least several years, whilst that between the Middle and Upper Units may have been on the order of tens of years.

The major variability in the tuff is in the degree of welding and the abundance of phenocryst phases. The most densely welded, eutaxitic, rocks are at the base of the Lower Unit (the basal vitrophyre; Fig. 3); the degree of welding increases upwards in both the Lower

and Middle Units. The content of quartz and feldspar phenocrysts increases upwards from 1% to 3% in both the Lower and Middle Units (Budding et al., 1987).

3. Samples and analytical methods

Budding et al. (1987) presented, for the Joe Lott Tuff, field observations, petrography and chemical analyses of whole-rocks and phenocrysts. Available for this study were their samples (U.S. Geological Survey collections; prefix M-) and additional material collected by the present authors in 2012 at the main sampling localities of Budding et al. (1987) (Fig. 1; prefix JLT-; details in Appendix 1).

Accessory phases were initially identified by SEM, using a Zeiss Σigma™ VP FE (variable pressure, field emission) SEM equipped with two Bruker XFlash 6|10™ energy-dispersive silicon drift detectors (SDD EDS). Identifications and images were acquired at 20 kV whereas mineral and glass compositions were determined using two electron probe microanalyzers, both using a 15 kv accelerating voltage. The φ(ρZ) correction model developed by Merlet (1994) was used for matrix corrections ("X-PHI correction model in the EPMA stock software – Peaksight).

Chevkinite and apatite compositions were determined using a Cameca SX-100 electron microprobe equipped with four wavelength dispersive spectrometers. Apatite was analysed with a 10 nA defocussed (5 μm) electron beam), where F and Cl were determined first, with a method of interception to initial time ("Time 0 intercept" from the subcounting options of Cameca's Peaksight software). Chevkinite and perrierite were analyzed with a fully focussed electron beam. A Cameca SXFiveFE microprobe equipped with five WDS spectrometers was used in determinations of monazite and matrix glass. Glass analyses were conducted with a 10

nA defocussed (20 μm) beam. Certain problems can arise with the analysis of glass, related especially to loss of volatiles. As well as compositional variations related to incomplete mixing of melts, glasses may be heterogeneous because of (i) proximity to different phenocrysts, and (ii) contamination by microlites. We have attempted to mitigate these problems by analyzing in sample M820 clear pools of matrix glass located as far as possible from phenocryst phases. Also, the glass analytical protocol was optimised by first measuring Na, F and Cl simultaneously, with the interception method to the initial time. Monazites were analyzed with different beam currents due to the differences in grain size. Common monazite and the carbon coating (20 nm) can withstand 10 minutes of a fully focussed 100 nA beam (or higher current up to 200 nA when defocussed accordingly) without experiencing internal damage or loss of the coating. Unfortunately, the host tuff matrix is susceptible to heat and loses volatiles, in our case the induced heat in monazite analyzed by a high current beam led to a carbon-coating bubble building around the monazite, culminating in an explosion resulting in a charging effect. Thus the beam current for the monazite analyses was on a point basis depending on the grain size, where the largest were analyzed at a few spots with a 150 nA defocussed (2 μm) beam, and the smallest at a single spot with a 20 nA fully focussed beam, as noted in Supplementary Table 2b.

The element standards, diffracting crystals, X-ray lines, overlap corrections, estimated detection limits, and standard deviations for glass and monazite are given in the Supplementary Materials.

Eight whole-rock samples, using powder splits from the Budding et al. (1987) collection, were analysed for major and trace elements at the Activation Laboratories Ltd, Ancaster, Canada. Major elements were determined by fusion-inductively coupled plasma spectrometry (FUS-ICP) and trace elements by combinations of FUS-ICP, fusion mass spectrometry (FUS-

MS) and total digestion inductively coupled plasma spectrometry (TD-ICP). Inductively coupled plasma-mass spectrometry (ICP-MS) and inductively coupled plasma-optical (ICP-OES) emission spectrometry were done using a lithium metaborate–tetraborate fusion procedure before sample dissolution. Analytical techniques are as follows: ICP-MS (Ag, Ce, Co, Cs, Dy, Er, Eu, Ga, Gd, Ge, Hf, Ho, La, Lu, Mo, Nb, Nd, Pb, Pr, Rb, Sm, Sn, Ta, Tb, Th, Tm, U, W, Y, and Yb); ICP-OES (major oxides, Ba, Be, Cu, Ni, Sr, V, Zn, and Zr), and loss on ignition (LOI) at 1000 °C. Quality control at Activation Laboratories is assessed by comparison with USGS, CANMET, and other appropriate in-house standards. Estimated uncertainty determined by duplicate, blank, and standard values is ≤±5% if the analyte is ≥10 × the detection limit and ±20% at the detection limit.

4. Petrography

The tuff contains about 1-3 vol% phenocrysts; most abundant is quartz, followed by sanidine and plagioclase, with lesser amounts of augite, biotite and FeTi-oxides (Table 1). The quartz is commonly heavily resorbed. The feldspars, up to 250 μm across, tend to be subhedral with some internal resorption. Plagioclase occurs in association with alkali feldspar in seven of the eight analysed samples, forming from 22-57% of the feldspar population. The compositional range is from $An_{24.7}Ab_{69.6}Or_{5.7}$ to $An_{11.6}Ab_{82.2}Or_{6.2}$) (Budding et al., 1987). Sanidine compositions range from $An_{2.9}Ab_{63.0}Or_{34.1}$ to $An_{0.7}Ab_{39.7}Or_{59.6}$. The clinopyroxene varies from $Ca_{44.9}Mg_{48.8}Fe_{6.4}$ to $Ca_{40.4}Mg_{43.0}Fe_{16.6}$ and is moderately aluminous (≤4.86 wt% Al_2O_3; 0.22 apfu). The feldspars and pyroxenes show no systematic compositional variation with stratigraphic height (Budding et al., 1987). According to Budding et al. (1987), apatite and zircon are present as accessories in all units, accompanied by allanite and a chevkinite-group mineral in the basal vitrophyre. The presence of allanite has not been confirmed in this

study, even in a re-examination of the Budding et al. thin sections. We note, however, that they found allanite in a mineral separate and its source is perhaps uncertain. In this study, monazite has been recorded in rocks from the Lower and Middle Units but was not indentified by Budding et al. (1987) in these Units.

The CGM occur as euhedral to subhedral crystals, rarely up to 65 μm across but more usually ≤20 μm. The forms vary from prismatic to platy; some are marginally and/or centrally resorbed (Fig. 4). Some 15-20 crystals are present in a standard thin section. The presence of a CGM as an inclusion in a large alkali feldspar phenocryst indicates that the phase was of relatively early-magmatic crystallization. While the CGM in sample M820 tend to be homogeneous, zonation from higher to lower Z on BSE images is common in sample M833. The crystal shown in Fig. 4a has a darker core with a lighter mantle, that in Fig. 4b shows indistinct sector zoning.

Monazite is a common microphenocryst; in sample M831, for example, 36 crystals have been identified in one thin section. Crystals range in size from 10 to 100 μm and occur in several forms: as discrete crystals (Fig. 5a), in clusters with, or mantled by, rutile, and in association with zircon (Fig. 5b) and magnetite (Fig. 5c). Resorption is common (Fig. 5d), zoning less so (Fig. 5c). There is no systematic compositional variation with stratigraphic height. Apatite is present in all samples, ranging from rare euhedral prismatic crystals up to 40 μm long (Fig. 6a) to isolated grains (Figs. 6b, c, d). As for monazite, there is no systematic compositional variation with stratigraphic height.

The basal vitrophyre contains four main varieties of glass (Fig. 7): (i) large- to medium-sized (≤2 cm long), partially collapsed, aphyric, brown or grey, fiamme and shards, commonly showing perlitic cracks (Gl 1); (ii) smaller, irregularly shaped brown, grey and white fiamme and shards (<1 cm long), occasionally with perlitic cracks (Gl 2); and (iii)

small, colourless fiamme (Gl 3); and (iv) the densely welded, sparsely porphyritic brown matrix glass.

The basal vitrophyre contains small amounts (2-4 per thin section) of black inclusions up to 4 mm across (Fig.8). The larger examples tend to be triangular in shape. A notable feature is that the inclusions have haloes, which are lighter-coloured than the host matrix glass (Fig. 8). The haloes appear to consist of complex mixtures of matrix glass, which sometimes takes on a yellowish colour, and devitrified zones comprising alkali feldspar and quartz (Fig. 8a). The inclusions commonly show internal zonation. That in Fig. 9b has a rim enriched in P (Fig. 8c), Ca (Fig. 8d) and S, and a concentric zonation in Fe, Na and K. The inclusions will be the subject of a separate study but the zonation must be the result of element diffusion within the inclusion. A possible interpretation is that the inclusions are enclaves, sufficiently hotter than the host glass to partially devitrify it in the haloes after eruption and to promote internal rearrangement. The P-Ca-enriched rim, presumably formed of apatite, strongly suggests that the enclaves had more mafic compositions than their host, which is P-poor (≤0.02 wt%; Table 2).

5. Whole-rock and matrix glass compositions

First, it must be noted that, as recognized by Budding et al. (1987), the rocks have been affected by post-emplacement redistribution of certain elements, especially Na, by devitrification and secondary hydration. The modifications are clearly shown in the high values of loss on ignition (0.94-5.57 wt%; Table 2), by the fact that Fe in the rocks is mainly present as Fe^{3+} (titrimetric determination; Budding et al., 1987) and by the peraluminous nature [A/(CNK): mol. $Al_2O_3/(CaO+Na_2O+K_2O)$ >1] of seven of the study rocks. In acknowledgment of the compositional modifications, element concentrations discussed in the text have been recalculated to 100 wt%, volatile-free. The compositional range is from

peraluminous to metaluminous but values have been affected by sodium loss. Given the phenocryst assemblage (quartz, sanidine, plagioclase, biotite, augite and FeTi-oxides), it is probable that the Joe Lott magmas were metaluminous.

The Joe Lott Tuff rhyolites are highly evolved compositionally: the summed values of CaO+MgO+FeO*+MnO+TiO_2 are ≤2.5 wt% (Table 2, recalculated to 100%). The tuff has a near-eutectic composition, in the sense that it plots close to low-pressure minima in the Quartz-Albite-Orthoclase system (Blundy and Cashman, 2001). The evolved nature is also shown in the rare earth element (REE) data); chondrite-normalized plots show strong light rare earth (LREE; La-Sm) enrichment ($[La/Yb]_{CN}$ 14.6-15.5, where CN is chondrite-normalized) and large Eu anomalies (Eu/Eu* 0.25-0.33) (Fig. 9). Nevertheless, the major and trace element abundances are all within the range of rhyolitic obsidians from continental interiors compiled by Macdonald et al. (1992), i.e. rocks of broadly similar tectonic setting. There appears to be no abnormal features about the tuff's composition that can be related to the CGM-monazite relationships.

Variations in major element compositions are generally small; the range of SiO_2 values, for example, is 75.4 to 76.7 wt% and that of Al_2O_3 from 12.2 to 13.1 wt%. Trace elements commonly show wider variations, e.g. Zr 125-210 ppm, Nb 30-41 and Sr 127-152 ppm. The ratios between geochemically coherent elements are also variable, e.g. Zr/Hf 23-32 and Nb/Ta 12-16.

Representative matrix glass analyses are given in Table 3 and the full data set in Supplementary Table 1. SiO_2 is in the range 73.4 to 75.8 wt% (75.2-78.6 wt%, recalculated to 100%). Apart from a positive correlation between SiO_2 and Al_2O_3, no pairs of elements show a significant correlation and it has not been possible to show the presence of discrete groups

of glass. Thus, the various forms of glass distinguished microscopically (Fig. 7) appear to be compositionally similar in major element terms.

6. Chemical composition of CGM, monazite-(Ce) and apatite-group minerals

6.1. Chevkinite-group minerals

Representative compositions of the CGM are given in Table 4 and the full data set is in Supplementary Table 2a. The analyses plot in the fields of the chevkinite and perrierite subgroups in the empirical classification scheme of Macdonald et al. (2009) (Fig. 10). Chevkinite-(Ce) occurs in the basal vitrophyre and perrierite-(Ce) in the Upper Unit (Fig. 3). The perrierite-(Ce) has higher contents of Al_2O_3, MnO, Hf, REE, Sc and Zr, and lower Th and U contents, than the chevkinite-(Ce). The highest ThO_2 contents in the chevkinite-(Ce) (7.15 wt%) are comparable to those recorded by Budding et al. (1987) and are the highest yet recorded in a CGM, with the exception of the so-called thoriochevkinite reported by Doelter (1931) from the Urals, Russia (20.9 wt%). Levels of ThO_2 in the perrierite-(Ce) are lower (1.32- 2.05 wt%). Abundances of UO_2 in the chevkinite-(Ce) are in the range 0.19-0.53 wt%; in the perrierite-(Ce) they are mostly below detection level. The lowest Th and U in the chevkinite-(Ce) are from an anomalously Nb-rich crystal (5.00 wt% Nb_2O_5). Abundances of Sc_2O_3 (≤0.39 wt%) and V_2O_3 (≤0.27 wt%), although low, are the highest recorded in chevkinite, according to the compilation of analyses by Macdonald et al. (2019a). Chondrite-normalized LREE patterns for the CGM (Fig. 11) show that the chevkinite-(Ce) and perrierite-(Ce) are very similar, although there are some small differences between them, e.g. $[La/Nd]_{CN}$ ranges from 2.7 to 3.5 and from 4.1 to 7.3, respectively. The monazite-(Ce) and

whole-rocks show broadly similar patterns (Figs. 9 and 11): $[La/Nd]_{CN}$ values range from 3.7 to 6.5 and 4.6 to 5.2, respectively.

Core to rim zonation in the perrierite-(Ce) crystal shown in Fig. 4a indicates a trend towards more "chevkinitic" composition, i.e. higher LREE and Y and lower Al_2O_3, CaO, Zr and Hf. Such zonation trends are thought to be a result of cooling differentiation (Macdonald et al., 2013, 2019a; Muhling et al., 2014).

6.2. Monazite-(Ce)

Representative compositions of monazite-(Ce) are given in Table 5: the full data set is in Supplementary Table 2b. The data lie between the huttonite ($REE^{3+} + P^{5+} = Th^{4+} + Si^{4+}$) and cheralite ($2REE^{3+} = Th^{4+} + Ca^{2+}$) compositional substitutions (Fig. 12). The chondrite-normalized patterns show strong LREE enrichment (Fig. 11), with some fractionation between elements, e.g. $[La/Nd]_{CN}$ 3.7 to 6.5. Abundances of FeO* are mainly <0.7 wt% but four analyses are in the range 1.1-2.1 wt%; they lie beneath the cheralite line on Fig. 12. Levels of ThO_2 reach ~17 wt%. A notable feature is the within-sample compositional range; in sample M830, for example, ThO_2 values range from 0.09-12.12 wt%, raising the possibility of mixed populations.

6.3. Apatite group

Representative apatite/fluorapatite compositions are given in Table 6; the full data set is in Supplementary Table 2c. The most important substituents are the LREE; the highest britholite component, judging from REE+Si contents is about 6%. Sodium and Fe are present in minor

amounts. Silica contents are up to 5.27 wt% (0.46 apfu) but it is possible that some higher values (≥0.15 apfu?) are due to beam contamination by quartz. The maximum Cl value is 1.01 wt%. Fluorine contents range from below detection to 4.5 wt% and are very variable within samples (Supplementary Table 2c).

We note that in stoichiometric fluorapatite the maximum F content is 3.77 wt%, yielding an apfu = 1for the X-site. Halogen diffusion during EPMA experiments can yield excess F values, as discussed by Goldoff et al. (2012) and Chakhmouradian et al. (2017). However, a coupled substitution $(PO_4)^{3-} \leftrightarrow (CO_3)^{2-} + F^-$, suggested by Yi et al. (2013), may allow F contents up to ~4.5 wt%. Definite assignment of specific species to particular crystallographic sites is beyond the scope of this paper.

There are significant compositional variations within samples: in sample M831, for example, Ce_2O_3 ranges from below detection to 0.91 wt% and in M833 from 0.18-0.98 wt%. The variability seems to be independent of the stratigraphic height of the samples. There is no totally systematic variation in any parameter with height either, except that the higher samples tend to have higher REE contents. It might be predicted that in a compositionally zoned reservoir certain elements would show a systematic distribution with temperature. In the Bishop Tuff apatites, for example, F and Y contents increased, and MgO and Cl contents decreased, with decreasing temperature (Hildreth, 1979).

7. Discussion

7.1. The Joe Lott magma system: conditions of crystallization

It is difficult to constrain the P-T conditions under which the tuff magma was stored and crystallized. There is a lack of suitable mineral pairs for geothermobarometry, such as two

oxides or two pyroxenes, and the use of clinopyroxene-melt or feldspar-melt pairs is precluded by post-emplacement modification of melt compositions, notably Na loss. Budding et al. (1987) suggested on the basis of plotting whole-rock data into the Quartz-Orthoclase-Albite system, that the pre-eruptive tuff was stored at ~0.8 ± 0.2 kbar pressure, under water-saturated conditions, at temperatures ranging from 750-770 °C. However, post-eruptive loss of Na has affected the normative Ab content of the magmas and thus their plotted positions. Nevertheless, the fact that the tuff is of high-silica composition and is saturated in quartz and feldspar indicates that the magma formed at low pressures, in the shallow crust (Blundy and Cashman, 2001, 2008; Gualda and Ghiorso, 2013). Furthermore, the temperatures are consistent with those estimated for other high-silica rhyolites: Fe-oxide temperatures of 720-790 °C for the Bishop Tuff were presented by Hildreth (1979), while the Zr-in-titanite method indicated temperatures possibly as low as 720 °C during crystallization of the high-silica part of the Peach Springs Tuff (Pamucku et al., 2013). Tierney et al. (2019) estimated that the high-silica portion of the Younger Toba Tuff crystallized at 700-740 °C.

The very low phenocryst abundances (≤3%) in the tuff seem to be at odds with the inferred low temperatures of formation and storage. They might infer that the magmas were very water-rich, with a corresponding lowering of crystallization temperatures. Possibly they point to highly efficient removal of melt from some underlying crystal mush with minimal subsequent crystal growth before eruption.

7.2. Was the Joe Lott reservoir compositionally zoned?

The Joe Lott Tuff is a highly fractionated magma body, of near-eutectic composition. In such compositions, trace elements can be a better guide to magma differentiation than major elements. The trace element abundances show some variability, e.g. Zr 125-210 ppm, Ba 56-193 ppm and Sr 27-152 ppm (Table 2). Ratios of geochemically coherent trace elements also

show small ranges, e.g. Zr/Hf 23-31 and Nb/Ta 11-16. In standard models of zoned magma chambers (Hildreth, 1981; Smith, 1979), many trace elements show coherent patterns of behaviour, being upward-concentrating or downward-concentrating, that is they are enriched or depleted in the higher, cooler parts of the reservoir. However, in the Joe Lott Tuff the trace elements more generally show variable patterns of behaviour. In the Lower Unit, for example, Ba and Rb are downward-concentrating but then both increase into the basal vitrophyre. In the Middle Unit, Ba increases in the same direction as Rb (Fig. 13; Table 2). The abundances of the LREE remain about constant in the Middle Unit, but are upward-concentrating in the Lower Unit, with a strong increase into the basal vitrophyre. If the magma reservoir was systematically compositionally zoned, the zoning was disturbed prior to, or during, eruption. It is possible that very active convection wiped out a subtle compositional zonation, the convection being promoted by an input of comparatively hot magma at a scale sufficiently large to partially homogenize the pre-eruptive chamber, as suggested by Huber et al. (2012) for the Southern Rocky Mountain volcanic field, or by overturn driven by gas exsolution (Bachmann and Bergantz, 2006). Little hybridization seems to have taken place, at least at the levels now represented in the tuff, the interaction between the injected and resident magmas being limited to heat transfer, as proposed for various magmatic systems by Bachmann et al. (2002), Bachmann and Bergantz (2006), Devine et al. (2003) and D'Oriano et al. (2017). A reheating event is consistent with the evidence of resorption in the feldspars, pyroxene, monazite and CGM and with the occurrence of inclusions interpreted above as magmatic enclaves.

Further evidence for disturbed compositional zonation may be the within-sample compositional ranges in the monazite-(Ce) and chevkinite-(Ce), and to a lesser degree in the apatite/fluorapatite data. The ranges of ThO_2 contents in monazite-(Ce) in samples M827 and

M831 are 0.2 to 7.6 wt% and 0.9 to 18.6 wt%, respectively (Table 5). A chevkinite-(Ce) in sample M830 has a Nb_2O_5 content of 5.0 wt% while all other analysed crystals have ≤0.8 wt% (Table 4). The variations may reflect mixing of crystals from different layers.

7.3. Distribution of CGM and monazite

There are records of monazite and CGM coexisting in the same rocks. Macdonald et al. (2016) reported monazite-(Ce) and chevkinite-(Ce) in a quartzolite from the Kola Peninsula, Russia. Both phases have been found in a Martian breccia meteorite (Liu et al., 2016). Monazite and chevkinite mantled by allanite were recorded by Li and Zhou (2017) in the Sin Quyen Fe-Cu-*LREE*-Au deposit, northwestern Vietnam. Miyawaki et al. (2012) found a CGM and monazite in volcanic rocks from Boso, Japan. However, the phases are not usually found together in igneous rocks. For example, in their comprehensive study of accessory mineral assemblages in 30 units of felsic volcanic rocks of the Timber Mountain-Oasis Valley caldera complex in Nevada, Broxton et al. (1989) recorded monazite and perrierite phenocrysts occurring together in only three units.

In the Joe Lott Tuff, chevkinite-(Ce) occurs in the basal vitrophyre and perrierite-(Ce) in the stratigraphically highest part of the Upper Unit. Intermediate facies contain monazite-(Ce). Such a relationship between CGM and monazite has not, to our knowledge, been recorded before in an igneous body. What caused the apparent changeovers? An increase in the activity of P, stabilizing the phosphate, can be ruled out: all rocks contain 0.02 wt% P_2O_5 (Table 2). An alternative possibility is varying Ca activity. The relative stabilities of allanite and monazite, for example, are related to the bulk contents of CaO, Al_2O_3 and Na_2O in the host rock, higher Ca activities resulting in allanite formation (Janots et al., 2008; Budzyń et

al., 2017). This can hardly be the case in the CGM/monazite relationships in the Joe Lott Tuff; values of A/CNK in the CGM-bearing units are 1.0-1.1, in the monazite-bearing units 1.0 - 1.2. A further possibility might have been pH_2O. It is highly likely that pH_2O increased downwards in the reservoir, perhaps promoting monazite growth, but we are unaware of any experimental evidence on this point.

7.4. Occurrence of perrierite in high-silica rhyolite

In igneous parageneses, perrierite is normally found in mafic and intermediate rocks. To our knowledge, it has not previously been confirmed in a high-silica rhyolite. McCurry (1988) reported it in the middle member of the rhyolitic Wild Horse Mesa Tuff, California (SiO_2 74.7-75.7 wt%), but no analysis was presented. Figure 14 shows that the Joe Lott perrierite-(Ce), along with selected samples from rocks of broadly trachyandesitic composition, plots in the field of CGM from mafic and intermediate rocks. The chevkinite-(Ce), in contrast, plots in or close to the field of CGM from evolved, oversaturated rocks.

The distribution of the CGM may be related to either a compositional effect or to differences in some important parameter or process in the pre-eruptive chamber. Perhaps the formation of perrierite-(Ce) was due to higher CaO and TiO_2 contents, and lower REE+Y contents, in the host melt than those in the chevkinite-(Ce)-bearing melt. However, sample M833 does have marginally lower REE+Y contents than sample M820 (160 and 170 ppm, respectively), but lower CaO (0.36, 0.82 wt%) and TiO_2 (0.14, 0.16 wt%) values (Table 2).

Alternatively, the perrierite-(Ce) may have been introduced by mixing of rhyolitic and trachyandesitic melts, as suggested by the presence of possible magmatic enclaves in the tuff. In their study of the pantelleritic Gold Flat Tuff, Black Mountain volcanic centre, Nevada,

Macdonald et al. (2019b) described a mixed-magma rock containing both chevkinite-(Ce) and perrierite-(Ce). In this case, and in contrast to the Joe Lott Tuff, the rock hosting both phases was clearly a mixture of rhyolitic and intermediate magmas. If the possibility, suggested above, that the pre-eruptive magma chamber underwent convective overturn is valid, the perrierite-(Ce) may have been introduced from a slightly deeper, hotter source than their current host, inferring that the crystallization of perrierite rather than chevkinite is controlled more by temperature than magma composition. The absence of a systematic distribution of fluorapatite compositions is also compatible with convective overturn.

Unusual features of the 150 km^3 Joe Lott Tuff include its near-eutectic composition, its crystal-poor nature and the non-systematic behaviour of many trace elements. We have attempted to use accessory minerals and whole-rock geochemistry to infer critical evidence of the magmatic evolution, such as the possible role of magma mixing. Further insights into the tuff will require an extensive vertical and lateral sampling programme, more detailed studies of textural/compositional relationships in the major phases, and additional studies of the accessory minerals, such as zircon and titanite.

8. Conclusions

(1) The high-silica rhyolitic Joe Lott Tuff has a volume of ~150 km^3, yet is compositionally homogeneous.

(2) The tuff was erupted from a compositionally zoned magma chamber where the zonation was disturbed by pre-eruptive convective overturn.

(3) The stratigraphically lowest and highest units contain phenocrysts of chevkinite-(Ce) and perrierite-(Ce), respectively, while intermediate units carry monazite-(Ce) phenocrysts.

(4) Both the CGM and monazite-(Ce) show significant inter-sample compositional variations which, along with the presence in the tuff of enclaves interpreted to have mafic-intermediate composition, are taken to suggest some mixing of the rhyolite with trachyandesitic (?) magma.

(5) No robust explanation is given as to why perrierite-(Ce) replaced chevkinite-(Ce) in the stratigraphically highest unit: it may have been related to the greater stability of perrierite-(Ce) at higher temperatures.

Acknowledgements

We thank Ms Lidia Jeżak for help in the electron microprobe laboratory and Marcin Syczewski for help with the SEM work. We also thank the late C. G. Cunningham (USGS retired) for access to the U.S. Geological Survey Joe Lott sample collection. The work was supported through the Innovative Economy Operational Program POIG.02.02.00-00-025/09 (NanoFun; Cryo-SEM microscopy lab). Financial support was also provided by the project BSt 185704 IGMiP.

References

Bachmann, O., Bergantz, G.W., 2006. Gas percolation in upper-crustal silicic crystal mushes as a mechanism for upward heat advection and rejuvenation of near-solidus magma bodies. Journal of Volcanology and Geothermal Research, 149, 85-102.

Bachmann, O, Dungan, M.A., Lipman, P.W., 2002. The Fish Canyon magma body, San

Juan volcanic field, Colorado: rejuvenation and eruption of an upper crustal batholith. Journal of Petrology, 43, 1469-1503.

Bagiński, B., Macdonald, R., 2013. The chevkinite group: underestimated accessory phases from a wide range of parageneses. Mineralogia, 44, 99-114.

Blundy, J., Cashman, K., 2001. Ascent-driven crystallization of dacite magmas at Mount St Helens, 1980-1986. Contributions to Mineralogy and Petrology, 140, 631-650.

Blundy, J., Cashman, K., 2008. Petrologic reconstruction of magmatic system variables and processes. Reviews of Mineralogy and Geochemistry, 69, 179-239.

Broxton, D.E., Warren, R.G., Byers, F.M., Scott, R.B., 1989. Chemical and mineralogic trends within the Timber Mountain-Oasis Valley caldera complex, Nevada: evidence for multiple cycles of chemical evolution in a long-lived silicic magma system. Journal of Geophysical Research, 94, 5961-5985.

Budding, K.E., Cunningham, C.G., Zielinski, R.A., Steven, T.A., Stern, C.R., 1987. Petrology and chemistry of the Joe Lott Tuff Member of the Mount Belknap Volcanics, Marysvale volcanic field, west-central Utah. U.S. Geological Survey Professional Paper, 2354, 47 pp.

Budzyń, B., Harlov, D.E., Kozub-Budzyń, G.A., Majka, J., 2017. Experimental constraints on the relative stabilities of the two systems monazite-(Ce) – allanite-(Ce) – fluorapatite and

xenotime-(Y) – (Y,HREE)-rich epidote – (Y,HREE-rich) fluorapatite, in high Ca and Na-Ca environments under P-T conditions of 200-1000 MPa and 450-750 °C. Mineralogy and Petrology, 111, 183-217.

Carlier, G., Lorand, J.-P., 2008. Zr-rich accessory minerals (titanite, perrierite, zirconolite, baddeleyite) record strong oxidation associated with magma mixing in the south Peruvian potassic province. Lithos, 104, 54-70.

Cellai, D., Conticelli, S., Diella, V., 1993. Perrierite-chevkinite in igneous ultrapotassic rocks from Central Italy: chemical data and their petrological significance. Periodico di Mineralogia, 62, 57-66.

Chakhmouradian, A.R., Reguir, E.P., Zaitsev, A.N., Couëslan, C., Xu, C., Kynicky, J., Mumin, A.H., Yang, P., 2107. Apatite in carbonatitic rocks: Compositional variation, zoning, element partitioning and petrogenetic significance. Lithos, 274, 188-213.

Cunningham, C.G., Steven, T.A., 1979. Mount Belknap and Red Hills calderas and associated rocks, Marysvale volcanic field, west-central Utah. U.S. Geological Survey Bulletin, 1468, 34 p.

de Hoog, J.C.M., van Bergen, M.J., 2000. Volatile-induced transport of HFSE, REE, Th and U in arc magmas: evidence from zirconolite-bearing vesicles in potassic lavas of Lewotolo volcano (Indonesia). Contributions to Mineralogy and Petrology, 139, 485-502.

Devine, J.D., Rutherford, M.J., Norton, G.E., Young, S.R., 2003. Magma storage region processes inferred from geochemistry of Fe-Ti oxides in andesitic magma, Soufriere Hills

volcano, Montserrat, WI. Journal of Petrology, 44, 1375-1400.

Doelter, C., 1931. Handbuch der Mineralchemie. Volume 3. Steinkopff; Dresden.

D'Oriano, C., Landi, P., Pimentel, A., Zanori, V., 2017. Magmatic processes revealed by anorthoclase textures and trace element modeling: The case of the Lajes Ignimbrite eruption (Terceira Island, Azores). Journal of Volcanology and Geothermal Research, 347, 44-63.

Goldoff, B., Webster, J.D., Harlov, D.E., 2017. Characterization of fluor-chlorapatites by electron probe microanalysis with a focus on time-dependent intensity variation of halogens. American Mineralogist, 97, 1103-1115.

Gualda, G.A.R., Ghiorso, M.S., 2013. Low-pressure origin of high-silica rhyolites and granites. Journal of Geology, 121, 537-545.

Hildreth, W., 1979. The Bishop Tuff: Evidence for the origin of compositional zonation in silicic magma chambers. Geological Society of America Special Paper, 180, 43-75.

Hildreth, W., 1981. Gradients in silicic magma chambers: implications for lithospheric magmatism. Journal of Geophysical Research, 86, 10153-10192.

Huber, C., Bachmann, O., Dufek, J., 2012. Crystal-poor versus crystal-rich ignimbrites: a competition between stirring and convection. Geology, 40, 115-118.

Janots, E., Engi, M., Berger, A., Allaz, J., Schwarz, J.O., Spandler, C., 2008. Prograde metamorphic sequence of REE minerals in politic rocks of the Central Alps: implications for allanite-monazite-xenotime phase relations from 250 to 610 °C. Journal of Metamorphic Geology, 26, 509-526.

Li, X.-C., Zhou, M.-F., 2017. Hydrothermal alteration of monazite-(Ce) and chevkinite-(Ce) from the Sin Quyen Fe-Cu-LREE-Au deposit, northwestern Vietnam. American Mineralogist, 102, 1525-1541.

Liu, Y., Ma, C., Beckett, J.R., Chen, Y., Guan, Y., 2016. Rare-earth-element minerals in martian breccia meteorites NWA 7034 and 7533: Implications for fluid-rock interaction in the martian crust. Earth and Planetary Science Letters, 451, 251-262.

Macdonald, R., Belkin, H.E., 2002. Compositional variation in minerals of the chevkinite group. Mineralogical Magazine, 66, 1075-1098.

Macdonald, R., Smith, R.L., Thomas, J.E., 1992. Chemistry of the subalkalic silicic obsidians. U.S. Geological Survey Professional Paper, **1523**, 214 pp.

Macdonald, R., Bagiński, B., Belkin, H.E., Dzierżanowski, P., Jeżak, L., 2008. REE partitioning between apatite and melt in a peralkaline volcanic suite, Kenya Rift Valley. Mineralogical Magazine, 72, 1147-1162.

Macdonald, R., Belkin, H.E., Wall, F., Bagiński, B., 2009. Compositional variation in the chevkinite group: new data from igneous and metamorphic rocks. Mineralogical Magazine, 73**,** 777-796.

Macdonald, R., Bagiński, B, Dzierżanowski, P., Fettes, D.J., Upton, B.G.J., 2013. Chevkinite-group minerals in UK Palaeogene granites: underestimated REE-bearing accessory phases. The Canadian Mineralogist, 51, 333-347.

Macdonald, R., Bagiński, B., Zozulya, D., 2017. Differing responses of zircon,

chevkinite-(Ce), monazite-(Ce) and fergusonite-(Y) to hydrothermal alteration: Evidence from the Keivy alkaline province, Kola Peninsula, Russia. Mineralogy and Petrology, 111, 523-545.

Macdonald, R., Bagiński, B., Belkin, H.E., Stachowicz, M., 2019a. Composition, paragenesis and alteration of the chevkinite group of minerals. American Mineralogist, 104, 349-367.

Macdonald, R., Bagiński, B., Belkin, H.E., White, J.C., Noble, D.C., 2019b. The Gold Flat Tuff, Nevada: insights into the evolution of peralkaline silicic magmas. Lithos, 328-329, 1-13.

McCurry, M., 1988. Geology and petrology of the Woods Mountain Volcanic Center, southeastern California: Implications for the genesis of peralkaline rhyolite ash flow tuffs. Journal of Geophysical Research, 93, 14835-14855.

Merlet, C. (1994) An accurate computer correction program for quantitative electron probe microanalysis. Microchimica Acta, 114, 363-376. https://doi.org/10.1007/BF01244563.

Miyawaki, R., Matsubara, S., Yokoyama, K., Momma, K., Sano, T., Tsutsumi, Y., Shigeoka, M., Nishikubo, K., 2012. Chevkinite-(Ce) in tuff at Heguri, Boso Peninsula, Chiba Prefecture, Japan. Bulletin of the National Museum of Natural Sciences, Ser. C, 38, 7-13.

Muhling, J.R., Suvorova, A.A., Rasmussen, B., 2014. The occurrence and composition of chevkinite-(Ce) and perrierite-(Ce) in tholeiitic intrusive rocks and lunar mare basalt.

American Mineralogist, 99, 1911-1921.

Pamukcu, A.S., Carley, T.L., Gualda, G.A.R., Miller, C.F., Ferguson, C.A., 2013. The evolution of the Peach Spring giant magma body: evidence from accessory mineral textures and compositions, bulk pumice and glass geochemistry, and rhyolite-MELTS modelling. Journal of Petrology, 54, 1109-1148.

Smith, R.L., 1979. Ash-flow magmatism. Geological Society of America Special Paper, 180, 5-27.

Sun, S.S., McDonough, W.F., 1989. Chemical and isotopic systematics of oceanic basalts: implications for mantle composition and processes. In: Saunders, A.D., Norry, M.J. (Eds.), Magmatism in the Ocean Basins, vol. 42, Geological Society, London, Special Publications, pp. 313-345.

Tierney, C.R., Reid, M.R., Vazquez, J.A., Chesner, C.A., 2019. Diverse late-stage crystallization and storage conditions in melt domains from the Youngest Toba Tuff revealed by age and compositional heterogeneity in the last increment of accessory phase growth. Contributions to Mineralogy and Petrology, 174, 31.

van Bergen, M.J., 1984. Perrierite in siliceous lavas from Mt Amiata, central Italy. Mineralogical Magazine, 48, 553-556.

Vlach, S.R.F., Gualda, G.A.R., 2007. Allanite and chevkinite in A-type granites and syenites of the Graciosa Province, southern Brazil. Lithos, 97, 98-121.

Wacaster, S., Streck, M.J., Belkin, H.E., Bodnar, R.J., 2011. Compositional zoning of the Devine Canyon Tuff, Oregon. American Geophysical Union, Fall Meeting 2011, abstract #V21C-2517.

Yi, H., Balan, E., Gervais, C., Segalen, L., Fayon, F., Roche, D., Person, A., Morin, G., Guillaumet, M., Blanchard, M., Lazzeri, M., Babonneau, F., 2013. A carbonate-fluoride defect model for carbonate-rich fluorapatite. American Mineralogist, 98, 1066–1069.

Figure captions

Fig. 1. Distribution of the Joe Lott Tuff and the location of samples (prefix JLT-) collected for this study by the authors at the sites marked by Budding et al. (1987); the latter samples are shown in Figure 3 (prefix M-) and the two sets of samples are correlated in Appendix 1.

Fig. 2. Joe Lott Tuff Member, exposed along State Route 4 at the eastern end of Clear Creek Canyon, where it is 138 m thick. The Lower, Middle and Upper cooling units are marked; the Pink cooling unit is absent from this locality (cf. Budding et al., 1987, fig. 5).

Fig. 3. Stratigraphic relationships in the Joe Lott Tuff Member, the underlying Bullion Canyon Volcanics and the overlying crystal-rich member of the Mount Belknap Volcanics (after Budding et al., 1987, fig. 4). The approximate positions of the Budding et al. samples (M-) are shown; the equivalent JLT- samples are listed in the Appendix and located in Figure 1. Also shown are the positions of samples containing CGM or monazite phenocrysts.

Fig. 4. Back-scattered electron (BSE) images of perrierite-(Ce) in sample M833. (a) Subhedral crystal with magmatic zonation. (b) Prism with partly preserved magmatic zonation and some internal resorption. Numbered spots refer to those in Supplementary Table 2.

Fig. 5. BSE images of monazite (Mnz). (a) Subhedral grains, with lighter rims in quartzofeldspathic matrix (Fsp). Sample M831A. (b) Enclosed in partially resorbed zircon phenocryst (Zrn), with fluorapatite (Ap) inclusion. Sample M830. (c) Anhedral crystals associated with magnetite phenocryst (Mag). Sample M830. (d) Aggregate of partially resorbed crystals. (b), (c) and (d) all enclosed in quartzofeldspathic matrix. Sample M831A. The letters on analysis spots refer to those in Supplementary Table 2.

Fig. 6. BSE images of fluorapatite (arrows). (a) Euhedral prism in coarsely devitrified matrix. Sample M827. (b) Aggregate of small anhedral crystals in coarsely devitrified matrix. Sample M833A. (c) Very small crystals typical of sample M832. Note glass shards and finely devitrified matrix. (d) Subhedral plate in devitrified matrix. Sample M833A.

Fig. 7. Photomicrograph of sample M820 from the basal vitrophyre. Three types of glass shards and pumice are marked (Gl 1, Gl 2, Gl 3). The main, brown, glass (the original ash component) is partly devitrified. Dark inclusion En 1 is shown in Fig. 8a. Inclusion En 2 is shown in Fig. 8b-d.

Fig. 8. (a) Photomicrograph of inclusion En 1 marked in Fig. 7. The glass shards around the inclusion have assumed a yellow colour. (b) BSE image of inclusion En 2 and the zonal arrangement around it. The outermost part shows small shards. It is followed by a grey zone which is mainly finely devitrified glass. The white rim encloses a dark central zone. (c) and (d) Compositional WDS X-ray maps of Ca and P in the inclusion, showing that the white rim is almost certainly formed of an apatite-group mineral.

Fig. 9. Chondrite-normalized REE patterns for whole-rocks. Data source: Table 2. Normalizing factors from Sun and McDonough (1989).

Fig. 10. Chevkinite-group minerals plotted in the FeO*-(CaO+SrO) discrimination diagram of Macdonald et al. (2009), where FeO* is total Fe as Fe^{2+}. CGM in sample M820 are chevkinite-(Ce), those in sample M833 are perrierite-(Ce). Also plotted are selected perrierites from volcanic rocks of broadly trachyandesitic composition: Lewotolo volcano, Indonesia (de Hoog and van Bergen, 2000), south Peruvian potassic province (Carlier and Lorand, 2008), Amiata volcano, Italy (van Bergen, 1984) and Montecatini Val de Cecina, Italy (Cellai et al., 1993).

Fig. 11. Chondrite-normalized REE patterns for CGM and monazite shown as fields. Data source: Supplementary Table 2. Normalizing factors from Sun and McDonough, 1989).

Fig. 12. Monazite compositions indicate substitution between the huttonite and cheralite mechanisms.

Fig. 13. Ba-Rb plot for rocks from the Lower (open circles) and Middle Units (solid circles). Arrows point towards stratigraphically higher samples in each unit.

Fig. 14. Triangular plot to show that chevkinite and perrierite generally tend to occur in different igneous lithologies. From Macdonald and Belkin (2002). The fields marked “evolved, undersaturated” and “evolved, oversaturated” are occupied only by chevkinite. The field marked mafic and intermediate igneous rocks includes only perrierite. Perrierite-(Ce) from the Joe Lott Tuff plots in the mafic and intermediate field, along with examples from the trachyandesites used in Figure 10, while the chevkinite-(Ce) plots in the evolved, oversaturated field.

Relationships between monazite, apatite and chevkinite-group minerals in the rhyolitic Joe Lott Tuff, Utah, USA

J. Galanciak[a], B. Bagiński[a,*], R. Macdonald[a,b], H. E. Belkin[c], J. Kotowski[a], P. Jokubauskas[a]

[a] Institute of Geochemistry, Mineralogy and Petrology, University of Warsaw, 02-089 Warszawa, Poland

[b] Environment Centre, Lancaster University, Lancaster LA1 4YQ, UK

[c] U.S. Geological Survey retired, 11142 Forest Edge Drive, Reston, VA 20190-4026, USA

° Corresponding author: e-mail B.Baginski1@uw.edu.pl

ABSTRACT

The high-silica rhyolitic Joe Lott Tuff was erupted at 19.2 ± 0.4 Ma from the Mount Belknap caldera in Utah, USA. Despite having a volume of ~150 km^3 it is compositionally homogeneous and contains ≤3 modal% phenocrysts. The tuff also shows two very unusual aspects of the REE-bearing phases, monazite and the chevkinite-group minerals (CGM): (i) the presence of perrierite-(Ce) in a high-silica rhyolite, and (ii) the replacement of CGM in the stratigraphic sequence by monazite, with a subsequent return to a CGM. Evidence from CGM distribution and variations in monazite and apatite-group composition with stratigraphic height in the deposit are used to infer that prior to eruption the magma was compositionally zoned, the zonation being partially obliterated by convective overturn in the reservoir.

KEYWORDS: Joe Lott Tuff; chevkinite-group; monazite; apatite-group; compositional zonation; convective overturn

1. Introduction

The Joe Lott Tuff Member of the Mount Belknap Volcanics is a high-silica rhyolitic ash flow tuff sheet associated with the collapse of the Mount Belknap caldera in west-central Utah at 19.2 ± 0.4 Ma (Fig. 1; Budding et al., 1987; Cunningham and Steven, 1979). The tuff has several unusual petrological features. High-silica rhyolitic eruptions greater than 1 km^3 in size are generally considered to be zoned compositionally and in phenocryst abundance, the zonation being reflected in the nature of the deposits (Hildreth, 1981; Smith, 1979). Despite its size, with a dense rock equivalent (DRE) volume of ~150 km^3, the Joe Lott Tuff is phenocryst-poor (1-3 modal%) and has a very homogeneous composition, e.g. 75.4 to 76.7 wt% SiO_2 (calculated 100%, volatile-free). We are unaware of any other ignimbrite of this volume of such uniformly high-silica composition and phenocryst-poor nature. For example, the Bishop Tuff, California, erupted at 0.7 Ma during formation of the Long Valley caldera, has a DRE volume of 170 km^3, phenocryst abundances ranging from 5 to 25 modal% and SiO_2 in the range ~75 to >77 wt% (Hildreth, 1979). The Devine Canyon Tuff, Oregon, has a minimum volume of 200 km^3 and SiO_2 contents in the range 74.6-77.6 wt%, but has phenocryst abundances ranging from 7 to 30 modal % (Wacaster et al., 2011). The high-silica portion (SiO_2 73-77 wt%) of the Younger Toba Tuff, Indonesia, has a volume >1000 km^3 and contains 12-25 wt% phenocrysts (Tierney et al., 2019).

In this study, we report on two further unusual features of the tuff. First, the presence in different units of phenocrysts of chevkinite-(Ce) and perrierite-(Ce), the most common members of the chevkinite-group of minerals (CGM; simplified formula [(REE, $Ca)_4Fe^{2+}(Fe^{2+},Fe^{3+},Ti,Al)_2Ti_2(Si_2O_7)_2$]), although these phases normally form in compositionally different igneous lithologies (Bagiński and Macdonald, 2013; Macdonald and Belkin, 2002; Macdonald et al., 2019a). Second, chevkinite-(Ce) and perrierite-(Ce) phenocrysts are absent from certain units, their place as the main REE-bearing phase being

taken by monazite ($REEPO_4$). So far as we are aware, this is the first record of such a relationship between these phases in an igneous body.

The specific aims are: (i) to document the occurrences and compositions of the CGM and monazite; (ii) to explain the occurrence of perrierite, rather than chevkinite, in a high-silica rhyolite; and (iii) to discuss the factors which controlled the distribution of the minerals. Data for the apatite-group phenocrysts are also included, to determine whether compositional variations in the monazite and CGM are mirrored by those in the apatite.

2. The Joe Lott Tuff

The Joe Lott Tuff Member of the Mount Belknap Volcanics is a composite sheet, changing laterally from a single cooling unit near source to four distinct cooling units distally (Fig. 2). Samples used in this study are all from outflow facies of the tuff. The Lower Unit is up to 64 m thick and has a basal vitrophyre. Initial collapse of the Mount Belknap caldera accompanied eruption of the Lower Unit (Fig. 3). The unit is followed upward by a Middle Unit up to 43 m thick, a 26 m pink-coloured unit, and an Upper Unit 31 m thick (Fig. 3). On the basis of the amount of erosion at the top of cooling units prior to eruption of the next unit, Budding et al. (1987) estimated that the time interval between the Lower and Middle Units was at least several years, whilst that between the Middle and Upper Units may have been on the order of tens of years.

The major variability in the tuff is in the degree of welding and the abundance of phenocryst phases. The most densely welded, eutaxitic, rocks are at the base of the Lower Unit (the basal vitrophyre; Fig. 3); the degree of welding increases upwards in both the Lower

and Middle Units. The content of quartz and feldspar phenocrysts increases upwards from 1% to 3% in both the Lower and Middle Units (Budding et al., 1987).

3. Samples and analytical methods

Budding et al. (1987) presented, for the Joe Lott Tuff, field observations, petrography and chemical analyses of whole-rocks and phenocrysts. Available for this study were their samples (U.S. Geological Survey collections; prefix M-) and additional material collected by the present authors in 2012 at the main sampling localities of Budding et al. (1987) (Fig. 1; prefix JLT-; details in Appendix 1).

Accessory phases were initially identified by SEM, using a Zeiss Σigma™ VP FE (variable pressure, field emission) SEM equipped with two Bruker XFlash 6|10™ energy-dispersive drift detectors (SDD EDS). Identifications and images were acquired at 20 kV whereas mineral and glass compositions were determined using two electron probe microanalyzers, both using a 15 kv accelerating voltage. The φ(ρZ) correction model developed by Merlet (1994) was used for matrix corrections ("X-PHI correction model in the EPMA stock software – Peaksight).

Chevkinite and apatite compositions were determined using a Cameca SX-100 electron microprobe equipped with four wavelength dispersive spectrometers. Apatite was analysed with a 10 nA defocussed (5 μm) electron beam), where F and Cl were determined first, with a method of interception to initial time ("Time 0 intercept" from the subcounting options of Cameca's Peaksight software). Chevkinite and perrierite were analyzed with a fully focussed electron beam. A Cameca SX-5 FE microprobe equipped with five WDS spectrometers was used in determinations of monazite and matrix glass. Glass analyses were conducted with a 10

nA defocussed (20 μm) beam. Certain problems can arise with the analysis of glass, related especially to Na volatility. As well as compositional variations related to incomplete mixing of melts, glasses may be heterogeneous because of (i) proximity to different phenocrysts, and (ii) contamination by microlites. We have attempted to mitigate these problems by analyzing in sample M820 clear pools of matrix glass located as far as possible from phenocryst phases. Also, the glass analytical protocol was optimised by first measuring Na, F and Cl simultaneously, with the interception method to the initial time. Monazites were analyzed with different beam currents due to the differences in grain size. Common monazite and the carbon coating (20 nm) can withstand 10 minutes of a fully focussed 100 nA beam (or higher current up to 200 nA when defocussed accordingly) without experiencing internal damage or loss of the coating. Unfortunately, the host tuff matrix is susceptible to heat and loses volatiles, in our case the induced heat in monazite analyzed by a high current beam led to a carbon-coating bubble building around the monazite, culminating in an explosion resulting in a charging effect. Thus the beam current for the monazite analyses was on a point basis depending on the grain size, where the largest were analyzed at a few spots with a 150 nA defocussed (2 μm) beam, and the smallest at a single spot with a 20 nA fully focussed beam, as noted in Supplementary Table 2b.

The element standards, diffracting crystals, X-ray lines, overlap corrections, estimated detection limits, and standard deviations are given in the Supplementary Materials.

Eight whole-rock samples, using powder splits from the Budding et al. (1987) collection, were analysed for major and trace elements at the Activation Laboratories Ltd, Ancaster, Canada. Major elements were determined by fusion-inductively coupled plasma spectrometry (FUS-ICP) and trace elements by combinations of FUS-ICP, fusion mass spectrometry (FUS-MS) and total digestion inductively coupled plasma spectrometry (TD-ICP). Inductively

coupled plasma-mass spectrometry (ICP-MS) and inductively coupled plasma-optical (ICP-OES) emission spectrometry were done using a lithium metaborate–tetraborate fusion procedure before sample dissolution. Analytical techniques are as follows: ICP-MS (Ag, Ce, Co, Cs, Dy, Er, Eu, Ga, Gd, Ge, Hf, Ho, La, Lu, Mo, Nb, Nd, Pb, Pr, Rb, Sm, Sn, Ta, Tb, Th, Tm, U, W, Y, and Yb); ICP-OES (major oxides, Ba, Be, Cu, Ni, Sr, V, Zn, and Zr), and loss on ignition (LOI) at 1000 °C. Quality control at Activation Laboratories is assessed by comparison with USGS, CANMET, and other appropriate in-house standards. Estimated uncertainty determined by duplicate, blank, and standard values is ≤±5% if the analyte is ≥10 × the detection limit and ±20% at the detection limit.

4. Petrography

The tuff contains about 1-3 vol% phenocrysts; most abundant is quartz, followed by sanidine and plagioclase, with lesser amounts of augite, biotite and FeTi-oxides (Table 1). The quartz is commonly heavily resorbed. The feldspars, up to 250 μm across, tend to be subhedral with some internal resorption. Plagioclase occurs in association with alkali feldspar in seven of the eight analysed samples, forming from 22-57% of the feldspar population. The compositional range is from $An_{24.7}Ab_{69.6}Or_{5.7}$ to $An_{11.6}Ab_{82.2}Or_{6.2}$) (Budding et al., 1987). Sanidine compositions range from $An_{2.9}Ab_{63.0}Or_{34.1}$ to $An_{0.7}Ab_{39.7}Or_{59.6}$. The clinopyroxene varies from $Ca_{44.9}Mg_{48.8}Fe_{6.4}$ to $Ca_{40.4}Mg_{43.0}Fe_{16.6}$ and is moderately aluminous (≤4.86 wt% Al_2O_3; 0.22 apfu). The feldspars and pyroxenes show no systematic compositional variation with stratigraphic height (Budding et al., 1987). According to Budding et al. (1987), apatite and zircon are present as accessories in all units, accompanied by allanite and a chevkinite-group mineral in the basal vitrophyre. The presence of allanite has not been confirmed in this study, even in a re-examination of the Budding et al. thin sections. We note, however, that

they found allanite in a mineral separate and its source is perhaps uncertain. In this study, monazite has been recorded in rocks from the Lower and Middle Units but was not indentified by Budding et al. (1987) in these Units.

The CGM occur as euhedral to subhedral crystals, rarely up to 65 μm across but more usually ≤20 μm. The forms vary from prismatic to platy; some are marginally and/or centrally resorbed (Fig. 4). Some 15-20 crystals are present in a standard thin section. The presence of a CGM as an inclusion in a large alkali feldspar phenocryst indicates that the phase was of relatively early-magmatic crystallization. While the CGM in sample M820 tend to be homogeneous, zonation from higher to lower Z on BSE images is common in sample M833. The crystal shown in Fig. 4a has a darker core with a lighter mantle, that in Fig. 4b shows indistinct sector zoning.

Monazite is a common microphenocryst; in sample M831, for example, 36 crystals have been identified in one thin section. Crystals range in size from 10 to 100 μm and occur in several forms: as discrete crystals (Fig. 5a), in clusters with, or mantled by, rutile, and in association with zircon (Fig. 5b) and magnetite (Fig. 5c). Resorption is common (Fig. 5d), zoning less so (Fig. 5c). There is no systematic compositional variation with stratigraphic height. Apatite is present in all samples, ranging from rare euhedral prismatic crystals up to 40 μm long (Fig. 6a) to isolated grains (Figs. 6b, c, d). As for monazite, there is no systematic compositional variation with stratigraphic height.

The basal vitrophyre contains four main varieties of glass (Fig. 7): (i) large- to medium-sized (≤2 cm long), partially collapsed, aphyric, brown or grey, fiamme and shards, commonly showing perlitic cracks (Gl 1); (ii) smaller, irregularly shaped brown, grey and white fiamme and shards (<1 cm long), occasionally with perlitic cracks (Gl 2); and (iii)

small, colourless fiamme (Gl 3); and (iv) the densely welded, sparsely porphyritic brown matrix glass.

The basal vitrophyre contains small amounts (2-4 per thin section) of black inclusions up to 4 mm across (Fig.8). The larger examples tend to be triangular in shape. A notable feature is that the inclusions have haloes, which are lighter-coloured than the host matrix glass (Fig. 8). The haloes appear to consist of complex mixtures of matrix glass, which sometimes takes on a yellowish colour, and devitrified zones comprising alkali feldspar and quartz (Fig. 8a). The inclusions commonly show internal zonation. That in Fig. 9b has a rim enriched in P (Fig. 8c), Ca (Fig. 8d) and S, and a concentric zonation in Fe, Na and K. The inclusions will be the subject of a separate study but the zonation must be the result of element diffusion within the inclusion. A possible interpretation is that the inclusions are enclaves, sufficiently hotter than the host glass to partially devitrify it in the haloes after eruption and to promote internal rearrangement. The P-Ca-enriched rim, presumably formed of apatite, strongly suggests that the enclaves had more mafic compositions than their host, which is P-poor (≤0.02 wt%; Table 2).

5. Whole-rock and matrix glass compositions

First, it must be noted that, as recognized by Budding et al. (1987), the rocks have been affected by post-emplacement redistribution of certain elements, especially Na, by devitrification and secondary hydration. The modifications are clearly shown in the high values of loss on ignition (0.94-5.57 wt%; Table 2), by the fact that Fe in the rocks is mainly present as Fe^{3+} (titrimetric determination; Budding et al., 1987) and by the peraluminous nature [A/(CNK): mol. $Al_2O_3/(CaO+Na_2O+K_2O)$ >1] of seven of the study rocks. In acknowledgment of the compositional modifications, element concentrations discussed in the text have been recalculated to 100 wt%, volatile-free. The compositional range is from

peraluminous to metaluminous but values have been affected by sodium loss. Given the phenocryst assemblage (quartz, sanidine, plagioclase, biotite, augite and FeTi-oxides), it is probable that the Joe Lott magmas were metaluminous.

The Joe Lott Tuff rhyolites are highly evolved compositionally: the summed values of CaO+MgO+FeO*+MnO+TiO_2 are ≤2.5 wt% (Table 2, recalculated to 100%). The tuff has a near-eutectic composition, in the sense that it plots close to low-pressure minima in the Quartz-Albite-Orthoclase system (Blundy and Cashman, 2001). The evolved nature is also shown in the rare earth element (REE) data); chondrite-normalized plots show strong light rare earth (LREE; La-Sm) enrichment ($[La/Yb]_{CN}$ 14.6-15.5, where CN is chondrite-normalized) and large Eu anomalies (Eu/Eu* 0.25-0.33) (Fig. 9). Nevertheless, the major and trace element abundances are all within the range of rhyolitic obsidians from continental interiors compiled by Macdonald et al. (1992), i.e. rocks of broadly similar tectonic setting. There appears to be no abnormal features about the tuff's composition that can be related to the CGM-monazite relationships.

Variations in major element compositions are generally small; the range of SiO_2 values, for example, is 75.4 to 76.7 wt% and that of Al_2O_3 from 12.2 to 13.1 wt%. Trace elements commonly show wider variations, e.g. Zr 125-210 ppm, Nb 30-41 and Sr 127-152 ppm. The ratios between geochemically coherent elements are also variable, e.g. Zr/Hf 23-32 and Nb/Ta 12-16.

Representative matrix glass analyses are given in Table 3 and the full data set in Supplementary Table 1. SiO_2 is in the range 73.4 to 75.8 wt% (75.2-78.6 wt%, recalculated to 100%). Apart from a positive correlation between SiO_2 and Al_2O_3, no pairs of elements show a significant correlation and it has not been possible to show the presence of discrete groups

of glass. Thus, the various forms of glass distinguished microscopically (Fig. 7) appear to be compositionally similar in major element terms.

6. Chemical composition of CGM, monazite-(Ce) and apatite-group minerals

6.1. Chevkinite-group minerals

Representative compositions of the CGM are given in Table 4 and the full data set is in Supplementary Table 2a. The analyses plot in the fields of the chevkinite and perrierite subgroups in the empirical classification scheme of Macdonald et al. (2009) (Fig. 10). Chevkinite-(Ce) occurs in the basal vitrophyre and perrierite-(Ce) in the Upper Unit (Fig. 3). The perrierite-(Ce) has higher contents of Al_2O_3, MnO, Hf, REE, Sc and Zr, and lower Th and U contents, than the chevkinite-(Ce). The highest ThO_2 contents in the chevkinite-(Ce) (7.15 wt%) are comparable to those recorded by Budding et al. (1987) and are the highest yet recorded in a CGM, with the exception of the so-called thoriochevkinite reported by Doelter (1931) from the Urals, Russia (20.9 wt%). Levels of ThO_2 in the perrierite-(Ce) are lower (1.32- 2.05 wt%). Abundances of UO_2 in the chevkinite-(Ce) are in the range 0.19-0.53 wt%; in the perrierite-(Ce) they are mostly below detection level. The lowest Th and U in the chevkinite-(Ce) are from an anomalously Nb-rich crystal (5.00 wt% Nb_2O_5). Abundances of Sc_2O_3 (≤0.39 wt%) and V_2O_3 (≤0.27 wt%), although low, are the highest recorded in chevkinite, according to the compilation of analyses by Macdonald et al. (2019a). Chondrite-normalized LREE patterns for the CGM (Fig. 11) show that the chevkinite-(Ce) and perrierite-(Ce) are very similar, although there are some small differences between them, e.g. $[La/Nd]_{CN}$ ranges from 2.7 to 3.5 and from 4.1 to 7.3, respectively. The monazite-(Ce) and

whole-rocks show broadly similar patterns (Figs. 9 and 11): $[La/Nd]_{CN}$ values range from 3.7 to 6.5 and 4.6 to 5.2, respectively.

Core to rim zonation in the perrierite-(Ce) crystal shown in Fig. 4a indicates a trend towards more "chevkinitic" composition, i.e. higher LREE and Y and lower Al_2O_3, CaO, Zr and Hf. Such zonation trends are thought to be a result of cooling differentiation (Macdonald et al., 2013, 2019a; Muhling et al., 2014).

6.2. Monazite-(Ce)

Representative compositions of monazite-(Ce) are given in Table 5: the full data set is in Supplementary Table 2b. The data lie between the huttonite ($REE^{3+} + P^{5+} = Th^{4+} + Si^{4+}$) and cheralite ($2REE^{3+} = Th^{4+} + Ca^{2+}$) compositional substitutions (Fig. 12). The chondrite-normalized patterns show strong LREE enrichment (Fig. 11), with some fractionation between elements, e.g. $[La/Nd]_{CN}$ 3.7 to 6.5. Abundances of FeO* are mainly <0.7 wt% but four analyses are in the range 1.1-2.1 wt%; they lie beneath the cheralite line on Fig. 12. Levels of ThO_2 reach ~17 wt%. A notable feature is the within-sample compositional range; in sample M830, for example, ThO_2 values range from 0.09-12.12 wt%, raising the possibility of mixed populations.

6.3. Apatite group

Representative apatite/fluorapatite compositions are given in Table 6; the full data set is in Supplementary Table 2c. The most important substituents are the LREE; the highest britholite component, judging from REE+Si contents is about 6%. Sodium and Fe are present in minor

amounts. Silica contents are up to 5.27 wt% (0.46 apfu) but it is possible that some higher values (≥0.15 apfu?) are due to beam contamination by quartz. The maximum Cl value is 1.01 wt%. Fluorine contents range from below detection to 4.5 wt% and are very variable within samples (Supplementary Table 2c). Analyzed apatite with low or nil Cl and/or F may suggest that these calcium phosphate apatites are dominated by hydroxylapatite component.

We note that in stoichiometric fluorapatite the maximum F content is 3.77 wt%, yielding an apfu = 1for the X-site. Halogen diffusion during EPMA experiments can yield excess F values, as discussed by Goldoff et al. (2012) and Chakhmouradian et al. (2017). However, a coupled substitution $(PO_4)^{3-} \leftrightarrow (CO_3)^{2-} + F^-$, suggested by Yi et al. (2013), may allow F contents up to ~4.5 wt%. Definite assignment of specific species to particular crystallographic sites is beyond the scope of this paper.

There are significant compositional variations within samples: in sample M831, for example, Ce_2O_3 ranges from below detection to 0.91 wt% and in M833 from 0.18-0.98 wt%. The variability seems to be independent of the stratigraphic height of the samples. There is no totally systematic variation in any parameter with height either, except that the higher samples tend to have higher REE contents. It might be predicted that in a compositionally zoned reservoir certain elements would show a systematic distribution with temperature. In the Bishop Tuff apatites, for example, F and Y contents increased, and MgO and Cl contents decreased, with decreasing temperature (Hildreth, 1979).

7. Discussion

7.1. The Joe Lott magma system: conditions of crystallization

It is difficult to constrain the P-T conditions under which the tuff magma was stored and crystallized. There is a lack of suitable mineral pairs for geothermobarometry, such as two oxides or two pyroxenes, and the use of clinopyroxene-melt or feldspar-melt pairs is precluded by post-emplacement modification of melt compositions, notably Na loss. Budding et al. (1987) suggested on the basis of plotting whole-rock data into the Quartz-Orthoclase-Albite system, that the pre-eruptive tuff was stored at ~0.8 ± 0.2 kbar pressure, under water-saturated conditions, at temperatures ranging from 750-770 °C. However, post-eruptive loss of Na has affected the normative Ab content of the magmas and thus their plotted positions. Nevertheless, the fact that the tuff is of high-silica composition and is saturated in quartz and feldspar indicates that the magma formed at low pressures, in the shallow crust (Blundy and Cashman, 2001, 2008; Gualda and Ghiorso, 2013). Furthermore, the temperatures are consistent with those estimated for other high-silica rhyolites: Fe-oxide temperatures of 720-790 °C for the Bishop Tuff were presented by Hildreth (1979), while the Zr-in-titanite method indicated temperatures possibly as low as 720 °C during crystallization of the high-silica part of the Peach Springs Tuff (Pamucku et al., 2013). Tierney et al. (2019) estimated that the high-silica portion of the Younger Toba Tuff crystallized at 700-740 °C.

The very low phenocryst abundances (≤3%) in the tuff seem to be at odds with the inferred low temperatures of formation and storage. They might infer that the magmas were very water-rich, with a corresponding lowering of crystallization temperatures. Possibly they point to highly efficient removal of melt from some underlying crystal mush with minimal subsequent crystal growth before eruption.

7.2. Was the Joe Lott reservoir compositionally zoned?

The Joe Lott Tuff is a highly fractionated magma body, of near-eutectic composition. In such compositions, trace elements can be a better guide to magma differentiation than major

elements. The trace element abundances show some variability, e.g. Zr 125-210 ppm, Ba 56-193 ppm and Sr 27-152 ppm (Table 2). Ratios of geochemically coherent trace elements also show small ranges, e.g. Zr/Hf 23-31 and Nb/Ta 11-16. In standard models of zoned magma chambers (Hildreth, 1981; Smith, 1979), many trace elements show coherent patterns of behaviour, being upward-concentrating or downward-concentrating, that is they are enriched or depleted in the higher, cooler parts of the reservoir. However, in the Joe Lott Tuff the trace elements more generally show variable patterns of behaviour. In the Lower Unit, for example, Ba and Rb are downward-concentrating but then both increase into the basal vitrophyre. In the Middle Unit, Ba increases in the same direction as Rb (Fig. 13; Table 2). The abundances of the LREE remain about constant in the Middle Unit, but are upward-concentrating in the Lower Unit, with a strong increase into the basal vitrophyre. If the magma reservoir was systematically compositionally zoned, the zoning was disturbed prior to, or during, eruption. It is possible that very active convection wiped out a subtle compositional zonation, the convection being promoted by an input of comparatively hot magma at a scale sufficiently large to partially homogenize the pre-eruptive chamber, as suggested by Huber et al. (2012) for the Southern Rocky Mountain volcanic field, or by overturn driven by gas exsolution (Bachmann and Bergantz, 2006). Little hybridization seems to have taken place, at least at the levels now represented in the tuff, the interaction between the injected and resident magmas being limited to heat transfer, as proposed for various magmatic systems by Bachmann et al. (2002), Bachmann and Bergantz (2006), Devine et al. (2003) and D'Oriano et al. (2017). A reheating event is consistent with the evidence of resorption in the feldspars, pyroxene, monazite and CGM and with the occurrence of inclusions interpreted above as magmatic enclaves.

Further evidence for disturbed compositional zonation may be the within-sample compositional ranges in the monazite-(Ce) and chevkinite-(Ce), and to a lesser degree in the apatite/fluorapatite data. The ranges of ThO_2 contents in monazite-(Ce) in samples M827 and M831 are 0.2 to 7.6 wt% and 0.9 to 18.6 wt%, respectively (Table 5). A chevkinite-(Ce) in sample M830 has a Nb_2O_5 content of 5.0 wt% while all other analysed crystals have ≤0.8 wt% (Table 4). The variations may reflect mixing of crystals from different layers.

7.3. Distribution of CGM and monazite

There are records of monazite and CGM coexisting in the same rocks. Macdonald et al. (2016) reported monazite-(Ce) and chevkinite-(Ce) in a quartzolite from the Kola Peninsula, Russia. Both phases have been found in a Martian breccia meteorite (Liu et al., 2016). Monazite and chevkinite mantled by allanite were recorded by Li and Zhou (2017) in the Sin Quyen Fe-Cu-*LREE*-Au deposit, northwestern Vietnam. Miyawaki et al. (2012) found a CGM and monazite in volcanic rocks from Boso, Japan. However, the phases are not usually found together in igneous rocks. For example, in their comprehensive study of accessory mineral assemblages in 30 units of felsic volcanic rocks of the Timber Mountain-Oasis Valley caldera complex in Nevada, Broxton et al. (1989) recorded monazite and perrierite phenocrysts occurring together in only three units.

In the Joe Lott Tuff, chevkinite-(Ce) occurs in the basal vitrophyre and perrierite-(Ce) in the stratigraphically highest part of the Upper Unit. Intermediate facies contain monazite-(Ce). Such a relationship between CGM and monazite has not, to our knowledge, been recorded before in an igneous body. What caused the apparent changeovers? An increase in the activity of P, stabilizing the phosphate, can be ruled out: all rocks contain 0.02 wt% P_2O_5

(Table 2). An alternative possibility is varying Ca activity. The relative stabilities of allanite and monazite, for example, are related to the bulk contents of CaO, Al_2O_3 and Na_2O in the host rock, higher Ca activities resulting in allanite formation (Janots et al., 2008; Budzyń et al., 2017). This can hardly be the case in the CGM/monazite relationships in the Joe Lott Tuff; values of A/CNK in the CGM-bearing units are 1.0-1.1, in the monazite-bearing units 1.0 - 1.2. A further possibility might have been pH_2O. It is highly likely that pH_2O increased downwards in the reservoir, perhaps promoting monazite growth, but we are unaware of any experimental evidence on this point.

7.4. Occurrence of perrierite in high-silica rhyolite

In igneous parageneses, perrierite is normally found in mafic and intermediate rocks. To our knowledge, it has not previously been confirmed in a high-silica rhyolite. McCurry (1988) reported it in the middle member of the rhyolitic Wild Horse Mesa Tuff, California (SiO_2 74.7-75.7 wt%), but no analysis was presented. Figure 14 shows that the Joe Lott perrierite-(Ce), along with selected samples from rocks of broadly trachyandesitic composition, plots in the field of CGM from mafic and intermediate rocks. The chevkinite-(Ce), in contrast, plots in or close to the field of CGM from evolved, oversaturated rocks.

The distribution of the CGM may be related to either a compositional effect or to differences in some important parameter or process in the pre-eruptive chamber. Perhaps the formation of perrierite-(Ce) was due to higher CaO and TiO_2 contents, and lower REE+Y contents, in the host melt than those in the chevkinite-(Ce)-bearing melt. However, sample M833 does have marginally lower REE+Y contents than sample M820 (160 and 170 ppm, respectively), but lower CaO (0.36, 0.82 wt%) and TiO_2 (0.14, 0.16 wt%) values (Table 2).

Alternatively, the perrierite-(Ce) may have been introduced by mixing of rhyolitic and trachyandesitic melts, as suggested by the presence of possible magmatic enclaves in the tuff. In their study of the pantelleritic Gold Flat Tuff, Black Mountain volcanic centre, Nevada, Macdonald et al. (2019b) described a mixed-magma rock containing both chevkinite-(Ce) and perrierite-(Ce). In this case, and in contrast to the Joe Lott Tuff, the rock hosting both phases was clearly a mixture of rhyolitic and intermediate magmas. If the possibility, suggested above, that the pre-eruptive magma chamber underwent convective overturn is valid, the perrierite-(Ce) may have been introduced from a slightly deeper, hotter source than their current host, inferring that the crystallization of perrierite rather than chevkinite is controlled more by temperature than magma composition. The absence of a systematic distribution of fluorapatite compositions is also compatible with convective overturn.

Unusual features of the 150 km^3 Joe Lott Tuff include its near-eutectic composition, its crystal-poor nature and the non-systematic behaviour of many trace elements. We have attempted to use accessory minerals and whole-rock geochemistry to infer critical evidence of the magmatic evolution, such as the possible role of magma mixing. Further insights into the tuff will require an extensive vertical and lateral sampling programme, more detailed studies of textural/compositional relationships in the major phases, and additional studies of the accessory minerals, such as zircon and titanite.

8. Conclusions

(1) The high-silica rhyolitic Joe Lott Tuff has a volume of ~150 km^3, yet is compositionally homogeneous.

(2) The tuff was erupted from a compositionally zoned magma chamber where the zonation was disturbed by pre-eruptive convective overturn.

(3) The stratigraphically lowest and highest units contain phenocrysts of chevkinite-(Ce) and perrierite-(Ce), respectively, while intermediate units carry monazite-(Ce) phenocrysts.

(4) Both the CGM and monazite-(Ce) show significant inter-sample compositional variations which, along with the presence in the tuff of enclaves interpreted to have mafic-intermediate composition, are taken to suggest some mixing of the rhyolite with trachyandesitic (?) magma.

(5) No robust explanation is given as to why perrierite-(Ce) replaced chevkinite-(Ce) in the stratigraphically highest unit: it may have been related to the greater stability of perrierite-(Ce) at higher temperatures.

Acknowledgements

We thank Ms Lidia Jeżak for help in the electron microprobe laboratory and Marcin Syczewski for help with the SEM work. Silvio Vlach and two anonymous reviewers provided very helpful, detailed, reviews of the manuscript. We also thank the late C. G. Cunningham (USGS retired) for access to the U.S. Geological Survey Joe Lott sample collection. The work was supported through the Innovative Economy Operational Program POIG.02.02.00-00-025/09 (NanoFun; Cryo-SEM microscopy lab). Financial support was also provided by the project BSt 185704 IGMiP.

References

Bachmann, O., Bergantz, G.W., 2006. Gas percolation in upper-crustal silicic crystal mushes as a mechanism for upward heat advection and rejuvenation of near-solidus magma bodies. Journal of Volcanology and Geothermal Research, 149, 85-102.

Bachmann, O, Dungan, M.A., Lipman, P.W., 2002. The Fish Canyon magma body, San Juan volcanic field, Colorado: rejuvenation and eruption of an upper crustal batholith. Journal of Petrology, 43, 1469-1503.

Bagiński, B., Macdonald, R., 2013. The chevkinite group: underestimated accessory phases from a wide range of parageneses. Mineralogia, 44, 99-114.

Blundy, J., Cashman, K., 2001. Ascent-driven crystallization of dacite magmas at Mount St Helens, 1980-1986. Contributions to Mineralogy and Petrology, 140, 631-650.

Blundy, J., Cashman, K., 2008. Petrologic reconstruction of magmatic system variables and processes. Reviews of Mineralogy and Geochemistry, 69, 179-239.

Broxton, D.E., Warren, R.G., Byers, F.M., Scott, R.B., 1989. Chemical and mineralogic trends within the Timber Mountain-Oasis Valley caldera complex, Nevada: evidence for multiple cycles of chemical evolution in a long-lived silicic magma system. Journal of Geophysical Research, 94, 5961-5985.

Budding, K.E., Cunningham, C.G., Zielinski, R.A., Steven, T.A., Stern, C.R., 1987. Petrology and chemistry of the Joe Lott Tuff Member of the Mount Belknap Volcanics,

Marysvale volcanic field, west-central Utah. U.S. Geological Survey Professional Paper, 2354, 47 pp.

Budzyń, B., Harlov, D.E., Kozub-Budzyń, G.A., Majka, J., 2017. Experimental constraints on the relative stabilities of the two systems monazite-(Ce) – allanite-(Ce) – fluorapatite and xenotime-(Y) – (Y,HREE)-rich epidote – (Y,HREE-rich) fluorapatite, in high Ca and Na-Ca environments under P-T conditions of 200-1000 MPa and 450-750 °C. Mineralogy and Petrology, 111, 183-217.

Carlier, G., Lorand, J.-P., 2008. Zr-rich accessory minerals (titanite, perrierite, zirconolite, baddeleyite) record strong oxidation associated with magma mixing in the south Peruvian potassic province. Lithos, 104, 54-70.

Cellai, D., Conticelli, S., Diella, V., 1993. Perrierite-chevkinite in igneous ultrapotassic rocks from Central Italy: chemical data and their petrological significance. Periodico di Mineralogia, 62, 57-66.

Chakhmouradian, A.R., Reguir, E.P., Zaitsev, A.N., Couëslan, C., Xu, C., Kynicky, J., Mumin, A.H., Yang, P., 2107. Apatite in carbonatitic rocks: Compositional variation, zoning, element partitioning and petrogenetic significance. Lithos, 274, 188-213.

Cunningham, C.G., Steven, T.A., 1979. Mount Belknap and Red Hills calderas and associated rocks, Marysvale volcanic field, west-central Utah. U.S. Geological Survey Bulletin, 1468, 34 p.

de Hoog, J.C.M., van Bergen, M.J., 2000. Volatile-induced transport of HFSE, REE, Th and U in arc magmas: evidence from zirconolite-bearing vesicles in potassic lavas of Lewotolo volcano (Indonesia). Contributions to Mineralogy and Petrology, 139, 485-502.

Devine, J.D., Rutherford, M.J., Norton, G.E., Young, S.R., 2003. Magma storage region processes inferred from geochemistry of Fe-Ti oxides in andesitic magma, Soufriere Hills volcano, Montserrat, WI. Journal of Petrology, 44, 1375-1400.

Doelter, C., 1931. Handbuch der Mineralchemie. Volume 3. Steinkopff; Dresden.

D'Oriano, C., Landi, P., Pimentel, A., Zanori, V., 2017. Magmatic processes revealed by anorthoclase textures and trace element modeling: The case of the Lajes Ignimbrite eruption (Terceira Island, Azores). Journal of Volcanology and Geothermal Research, 347, 44-63.

Goldoff, B., Webster, J.D., Harlov, D.E., 2017. Characterization of fluor-chlorapatites by electron probe microanalysis with a focus on time-dependent intensity variation of halogens. American Mineralogist, 97, 1103-1115.

Gualda, G.A.R., Ghiorso, M.S., 2013. Low-pressure origin of high-silica rhyolites and granites. Journal of Geology, 121, 537-545.

Hildreth, W., 1979. The Bishop Tuff: Evidence for the origin of compositional zonation in silicic magma chambers. Geological Society of America Special Paper, 180, 43-75.

Hildreth, W., 1981. Gradients in silicic magma chambers: implications for lithospheric magmatism. Journal of Geophysical Research, 86, 10153-10192.

Huber, C., Bachmann, O., Dufek, J., 2012. Crystal-poor versus crystal-rich ignimbrites: a competition between stirring and convection. Geology, 40, 115-118.

Janots, E., Engi, M., Berger, A., Allaz, J., Schwarz, J.O., Spandler, C., 2008. Prograde metamorphic sequence of REE minerals in politic rocks of the Central Alps: implications for allanite-monazite-xenotime phase relations from 250 to 610 °C. Journal of Metamorphic Geology, 26, 509-526.

Li, X.-C., Zhou, M.-F., 2017. Hydrothermal alteration of monazite-(Ce) and chevkinite-(Ce) from the Sin Quyen Fe-Cu-LREE-Au deposit, northwestern Vietnam. American Mineralogist, 102, 1525-1541.

Liu, Y., Ma, C., Beckett, J.R., Chen, Y., Guan, Y., 2016. Rare-earth-element minerals in martian breccia meteorites NWA 7034 and 7533: Implications for fluid-rock interaction in the martian crust. Earth and Planetary Science Letters, 451, 251-262.

Macdonald, R., Belkin, H.E., 2002. Compositional variation in minerals of the chevkinite group. Mineralogical Magazine, 66, 1075-1098.

Macdonald, R., Smith, R.L., Thomas, J.E., 1992. Chemistry of the subalkalic silicic obsidians. U.S. Geological Survey Professional Paper, **1523**, 214 pp.

Macdonald, R., Bagiński, B., Belkin, H.E., Dzierżanowski, P., Jeżak, L., 2008. REE partitioning between apatite and melt in a peralkaline volcanic suite, Kenya Rift Valley. Mineralogical Magazine, 72, 1147-1162.

Macdonald, R., Belkin, H.E., Wall, F., Bagiński, B., 2009. Compositional variation in the chevkinite group: new data from igneous and metamorphic rocks. Mineralogical Magazine, 73**,** 777-796.

Macdonald, R., Bagiński, B, Dzierżanowski, P., Fettes, D.J., Upton, B.G.J., 2013. Chevkinite-group minerals in UK Palaeogene granites: underestimated REE-bearing accessory phases. The Canadian Mineralogist, 51, 333-347.

Macdonald, R., Bagiński, B., Zozulya, D., 2017. Differing responses of zircon, chevkinite-(Ce), monazite-(Ce) and fergusonite-(Y) to hydrothermal alteration: Evidence from the Keivy alkaline province, Kola Peninsula, Russia. Mineralogy and Petrology, 111, 523-545.

Macdonald, R., Bagiński, B., Belkin, H.E., Stachowicz, M., 2019a. Composition, paragenesis and alteration of the chevkinite group of minerals. American Mineralogist, 104, 349-367.

Macdonald, R., Bagiński, B., Belkin, H.E., White, J.C., Noble, D.C., 2019b. The Gold Flat Tuff, Nevada: insights into the evolution of peralkaline silicic magmas. Lithos, 328-329, 1-13.

McCurry, M., 1988. Geology and petrology of the Woods Mountain Volcanic Center, southeastern California: Implications for the genesis of peralkaline rhyolite ash flow tuffs. Journal of Geophysical Research, 93, 14835-14855.

Merlet, C. (1994) An accurate computer correction program for quantitative electron probe microanalysis. Microchimica Acta, 114, 363-376. https://doi.org/10.1007/BF01244563.

Miyawaki, R., Matsubara, S., Yokoyama, K., Momma, K., Sano, T., Tsutsumi, Y., Shigeoka,

M., Nishikubo, K., 2012. Chevkinite-(Ce) in tuff at Heguri, Boso Peninsula, Chiba Prefecture, Japan. Bulletin of the National Museum of Natural Sciences, Ser. C, 38, 7-13.

Muhling, J.R., Suvorova, A.A., Rasmussen, B., 2014. The occurrence and composition of chevkinite-(Ce) and perrierite-(Ce) in tholeiitic intrusive rocks and lunar mare basalt. American Mineralogist, 99, 1911-1921.

Pamukcu, A.S., Carley, T.L., Gualda, G.A.R., Miller, C.F., Ferguson, C.A., 2013. The evolution of the Peach Spring giant magma body: evidence from accessory mineral textures and compositions, bulk pumice and glass geochemistry, and rhyolite-MELTS modelling. Journal of Petrology, 54, 1109-1148.

Smith, R.L., 1979. Ash-flow magmatism. Geological Society of America Special Paper, 180, 5-27.

Sun, S.S., McDonough, W.F., 1989. Chemical and isotopic systematics of oceanic basalts: implications for mantle composition and processes. In: Saunders, A.D., Norry, M.J. (Eds.), Magmatism in the Ocean Basins, vol. 42, Geological Society, London, Special Publications, pp. 313-345.

Tierney, C.R., Reid, M.R., Vazquez, J.A., Chesner, C.A., 2019. Diverse late-stage crystallization and storage conditions in melt domains from the Youngest Toba Tuff revealed by age and compositional heterogeneity in the last increment of accessory phase

growth. Contributions to Mineralogy and Petrology, 174, 31.

van Bergen, M.J., 1984. Perrierite in siliceous lavas from Mt Amiata, central Italy. Mineralogical Magazine, 48, 553-556.

Vlach, S.R.F., Gualda, G.A.R., 2007. Allanite and chevkinite in A-type granites and syenites of the Graciosa Province, southern Brazil. Lithos, 97, 98-121.

Wacaster, S., Streck, M.J., Belkin, H.E., Bodnar, R.J., 2011. Compositional zoning of the Devine Canyon Tuff, Oregon. American Geophysical Union, Fall Meeting 2011, abstract #V21C-2517.

Yi, H., Balan, E., Gervais, C., Segalen, L., Fayon, F., Roche, D., Person, A., Morin, G., Guillaumet, M., Blanchard, M., Lazzeri, M., Babonneau, F., 2013. A carbonate-fluoride defect model for carbonate-rich fluorapatite. American Mineralogist, 98, 1066–1069.

Figure captions

Fig. 1. Distribution of the Joe Lott Tuff and the location of samples (prefix JLT-) collected for this study by the authors at the sites marked by Budding et al. (1987); the latter samples are shown in Figure 3 (prefix M-) and the two sets of samples are correlated in Appendix 1.

Fig. 2. Joe Lott Tuff Member, exposed along State Route 4 at the eastern end of Clear Creek Canyon, where it is 138 m thick. The Lower, Middle and Upper cooling units are marked; the Pink cooling unit is absent from this locality (cf. Budding et al., 1987, fig. 5).

Fig. 3. Stratigraphic relationships in the Joe Lott Tuff Member, the underlying Bullion Canyon Volcanics and the overlying crystal-rich member of the Mount Belknap Volcanics (after Budding et al., 1987, fig. 4). The approximate positions of the Budding et al. samples (M-) are shown; the equivalent JLT- samples are listed in the Appendix and located in Figure 1. Also shown are the positions of samples containing CGM or monazite phenocrysts.

Fig. 4. Back-scattered electron (BSE) images of perrierite-(Ce) in sample M833. (a) Subhedral crystal with magmatic zonation. (b) Prism with partly preserved magmatic zonation and some internal resorption. Numbered spots refer to those in Supplementary Table 2.

Fig. 5. BSE images of monazite (Mnz). (a) Subhedral grains, with lighter rims in quartzofeldspathic matrix (Fsp). Sample M831A. (b) Enclosed in partially resorbed zircon phenocryst (Zrn), with fluorapatite (Ap) inclusion. Sample M830. (c) Anhedral crystals associated with magnetite phenocryst (Mag). Sample M830. (d) Aggregate of partially resorbed crystals. (b), (c) and (d) all enclosed in quartzofeldspathic matrix. Sample M831A. The letters on analysis spots refer to those in Supplementary Table 2.

Fig. 6. BSE images of fluorapatite (arrows). (a) Euhedral prism in coarsely devitrified matrix. Sample M827. (b) Aggregate of small anhedral crystals in coarsely devitrified matrix. Sample M833A. (c) Very small crystals typical of sample M832. Note glass shards and finely devitrified matrix. (d) Subhedral plate in devitrified matrix. Sample M833A.

Fig. 7. Photomicrograph of sample M820 from the basal vitrophyre. Three types of glass shards and pumice are marked (Gl 1, Gl 2, Gl 3). The main, brown, glass (the original ash component) is partly devitrified. Dark inclusion En 1 is shown in Fig. 8a. Inclusion En 2 is shown in Fig. 8b-d.

Fig. 8. (a) Photomicrograph of inclusion En 1 marked in Fig. 7. The glass shards around the inclusion have assumed a yellow colour. (b) BSE image of inclusion En 2 and the zonal arrangement around it. The outermost part shows small shards. It is followed by a grey zone which is mainly finely devitrified glass. The white rim encloses a dark central zone. (c) and (d) Compositional WDS X-ray maps of Ca and P in the inclusion, showing that the white rim is almost certainly formed of an apatite-group mineral.

Fig. 9. Chondrite-normalized REE patterns for whole-rocks. Data source: Table 2. Normalizing factors from Sun and McDonough (1989).

Fig. 10. Chevkinite-group minerals plotted in the FeO*-(CaO+SrO) discrimination diagram of Macdonald et al. (2009), where FeO* is total Fe as Fe^{2+}. CGM in sample M820 are chevkinite-(Ce), those in sample M833 are perrierite-(Ce). Also plotted are selected perrierites from volcanic rocks of broadly trachyandesitic composition: Lewotolo volcano, Indonesia (de Hoog and van Bergen, 2000), south Peruvian potassic province (Carlier and Lorand, 2008), Amiata volcano, Italy (van Bergen, 1984) and Montecatini Val de Cecina, Italy (Cellai et al., 1993).

Fig. 11. Chondrite-normalized REE patterns for CGM and monazite shown as fields. Data source: Supplementary Table 2. Normalizing factors from Sun and McDonough, 1989).

Fig. 12. Monazite compositions indicate substitution between the huttonite and cheralite mechanisms.

Fig. 13. Ba-Rb plot for rocks from the Lower (open circles) and Middle Units (solid circles). Arrows point towards stratigraphically higher samples in each unit.

Fig. 14. Triangular plot to show that chevkinite and perrierite generally tend to occur in different igneous lithologies. From Macdonald and Belkin (2002). The fields marked

“evolved, undersaturated” and “evolved, oversaturated” are occupied only by chevkinite. The field marked mafic and intermediate igneous rocks includes only perrierite. Perrierite-(Ce) from the Joe Lott Tuff plots in the mafic and intermediate field, along with examples from the trachyandesites used in Figure 10, while the chevkinite-(Ce) plots in the evolved, oversaturated field.

Figure 1

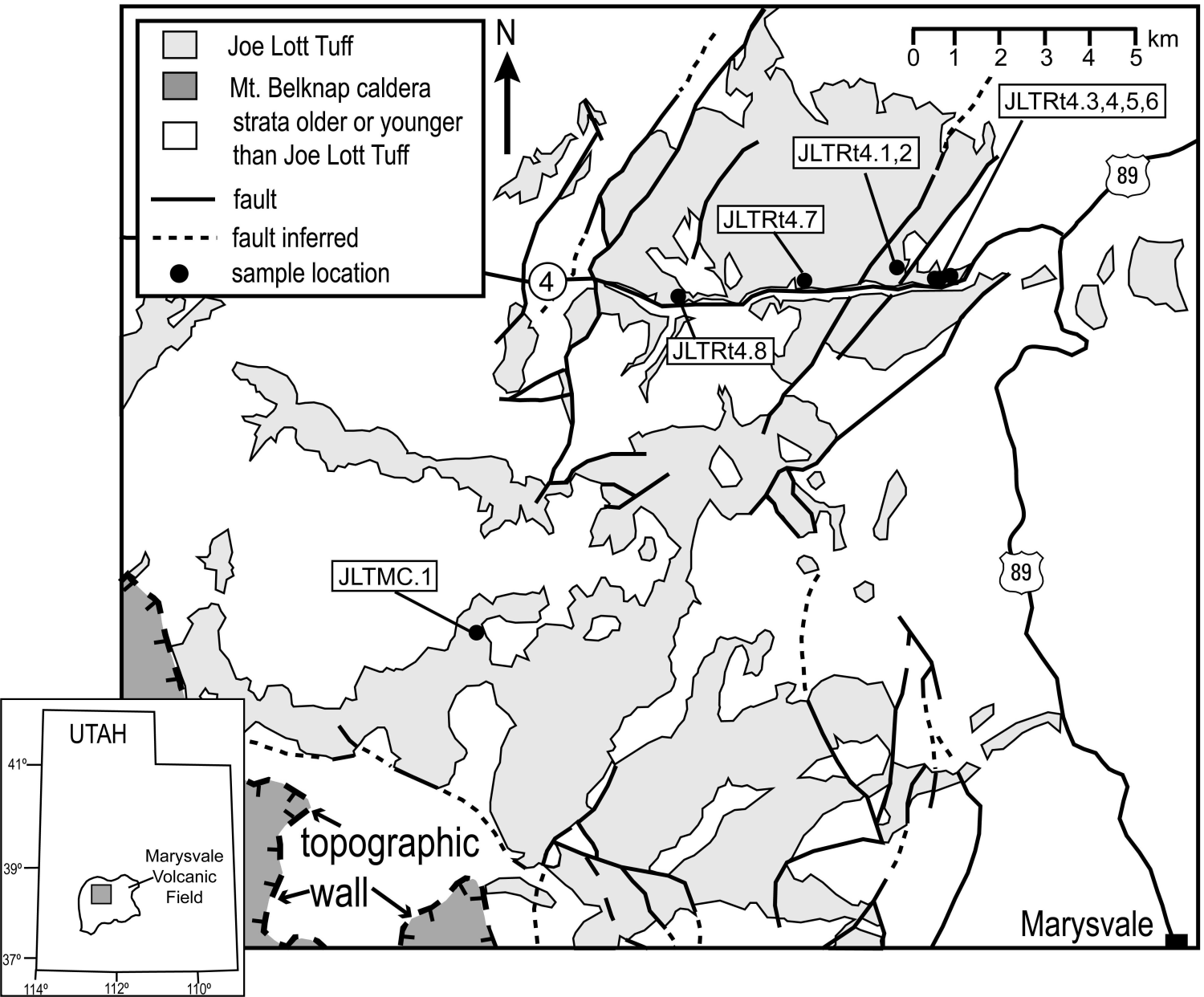
Joe Lott Tuff
Mt. Belknap caldera
strata older or younger than Joe Lott Tuff
fault
fault inferred
sample location
N
0 1 2 3 4 5 km
JLTRt4.3,4,5,6
JLTRt4.1,2
JLTRt4.7
JLTRt4.8
JLTMC.1
4
89
89
topographic wall
Marysvale
UTAH
41°
39°
37°
114°
112°
110°
Marysvale Volcanic Field

Figure 2

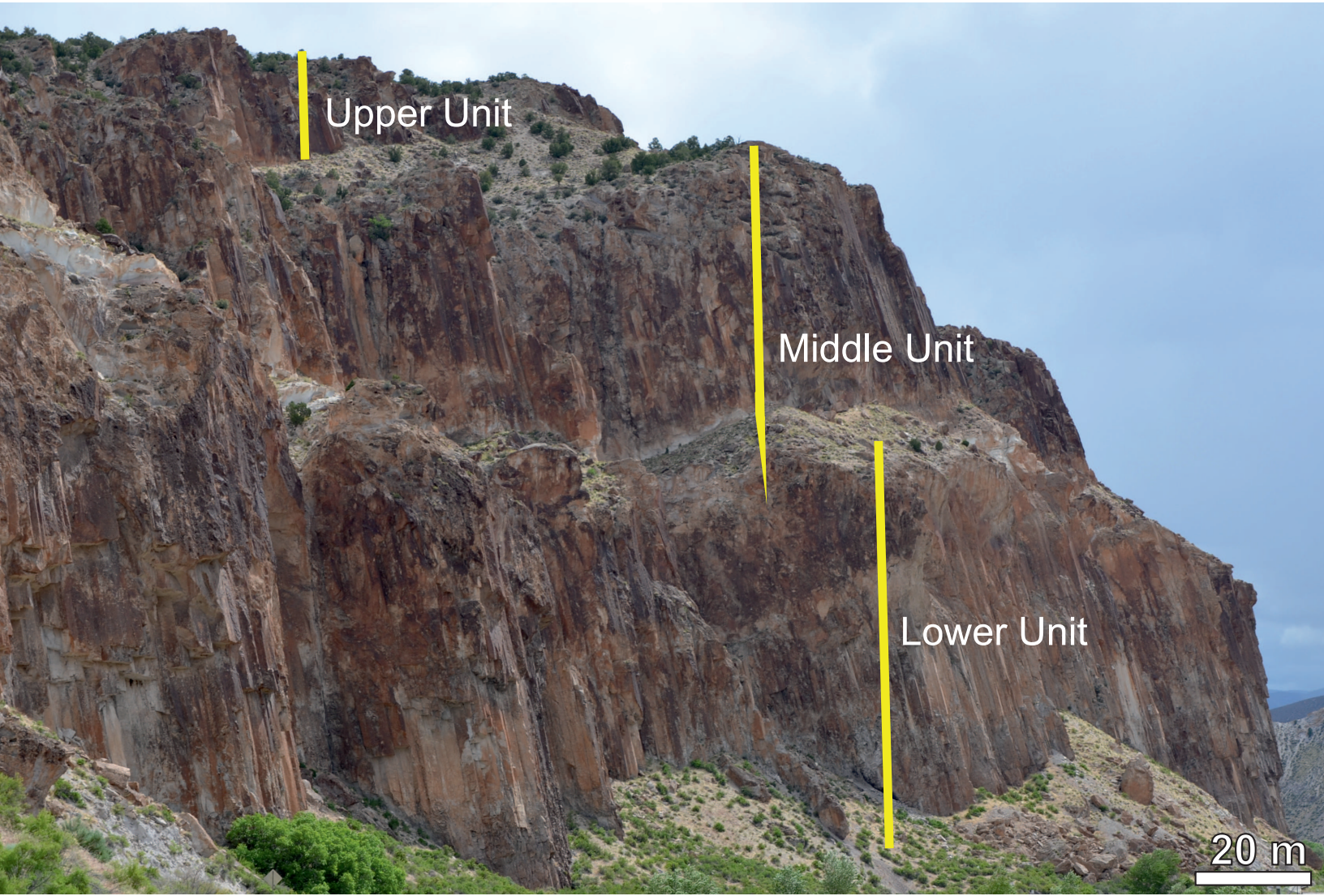

Figure 3

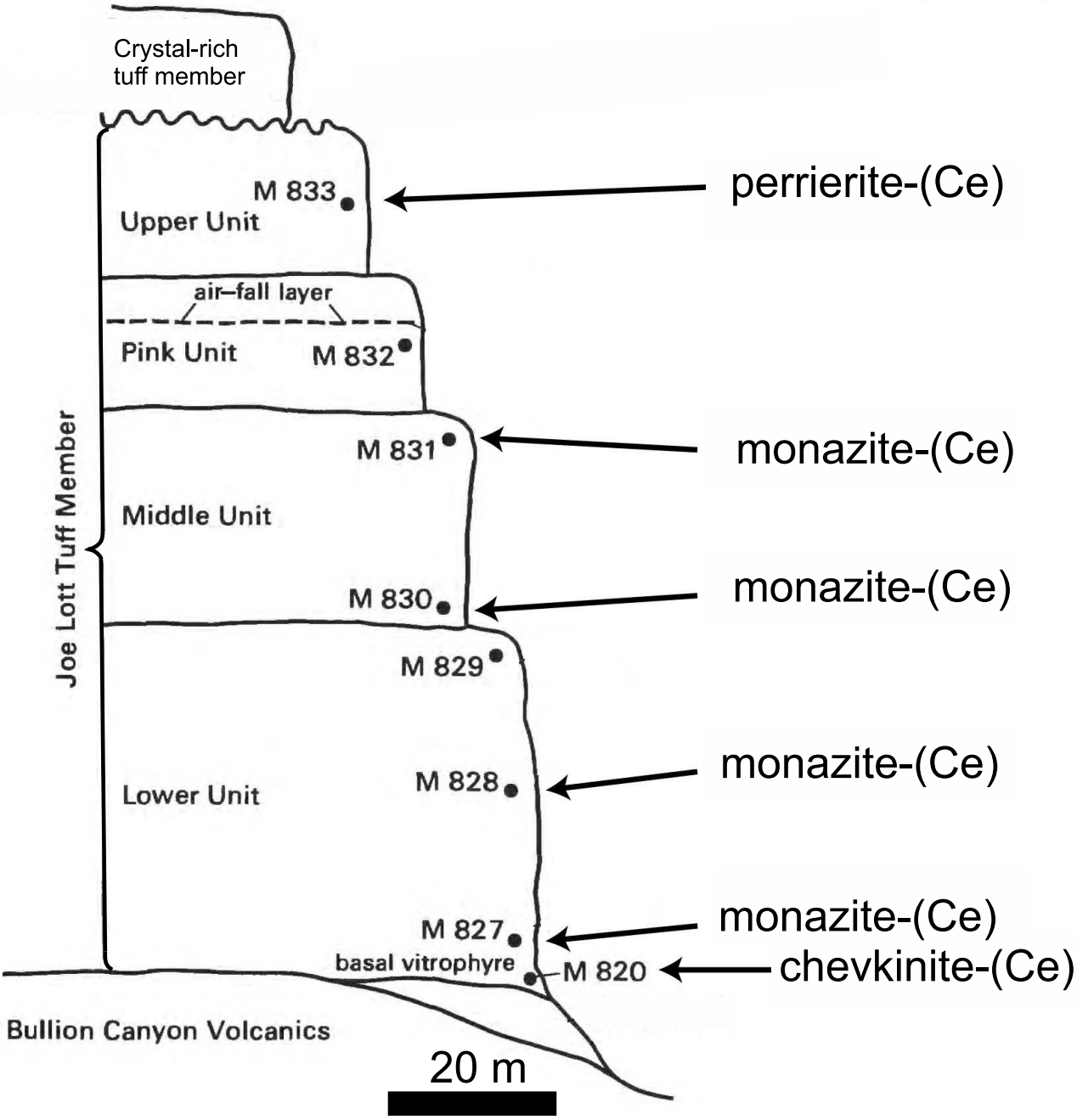
Crystal-rich
tuff member
M 833
Upper Unit
perrierite-(Ce)
air–fall layer
Pink Unit
M 832
M 831
monazite-(Ce)
Middle Unit
Joe Lott Tuff Member
M 830
monazite-(Ce)
M 829
M 828
monazite-(Ce)
Lower Unit
M 827
monazite-(Ce)
basal vitrophyre
M 820
chevkinite-(Ce)
Bullion Canyon Volcanics
20 m

Figure 4

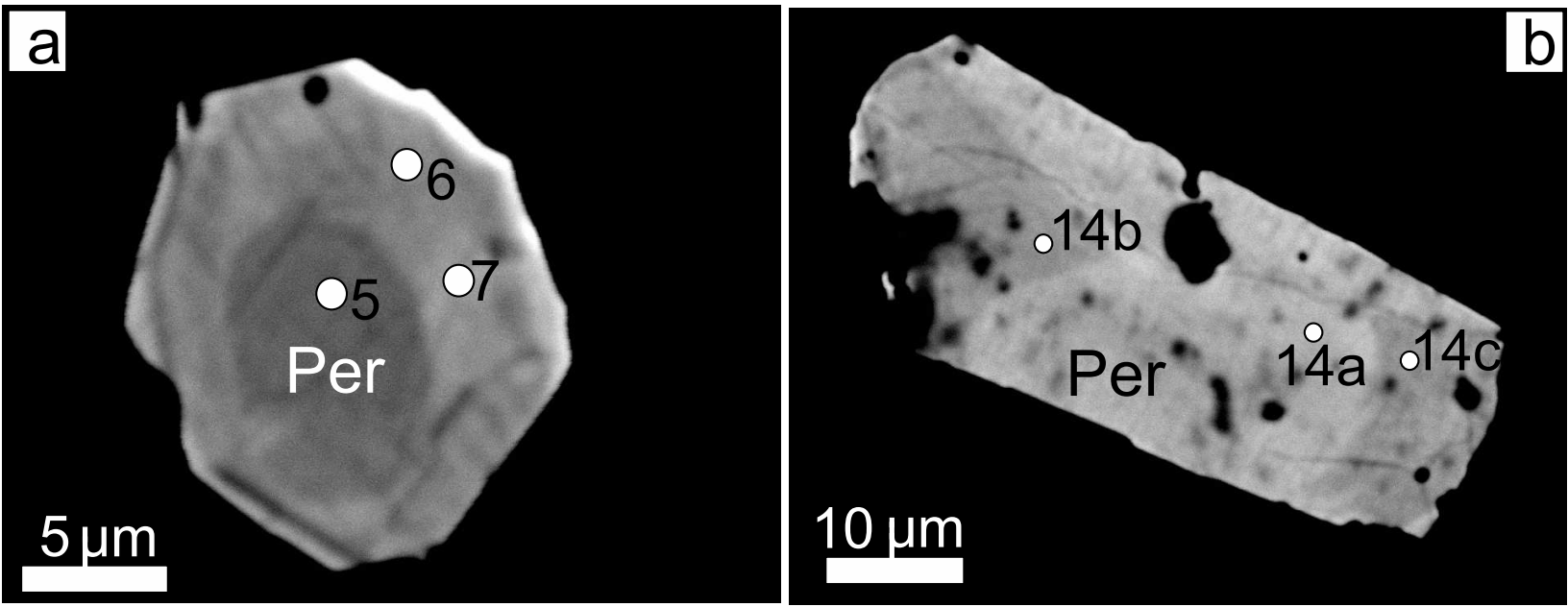

Figure 5

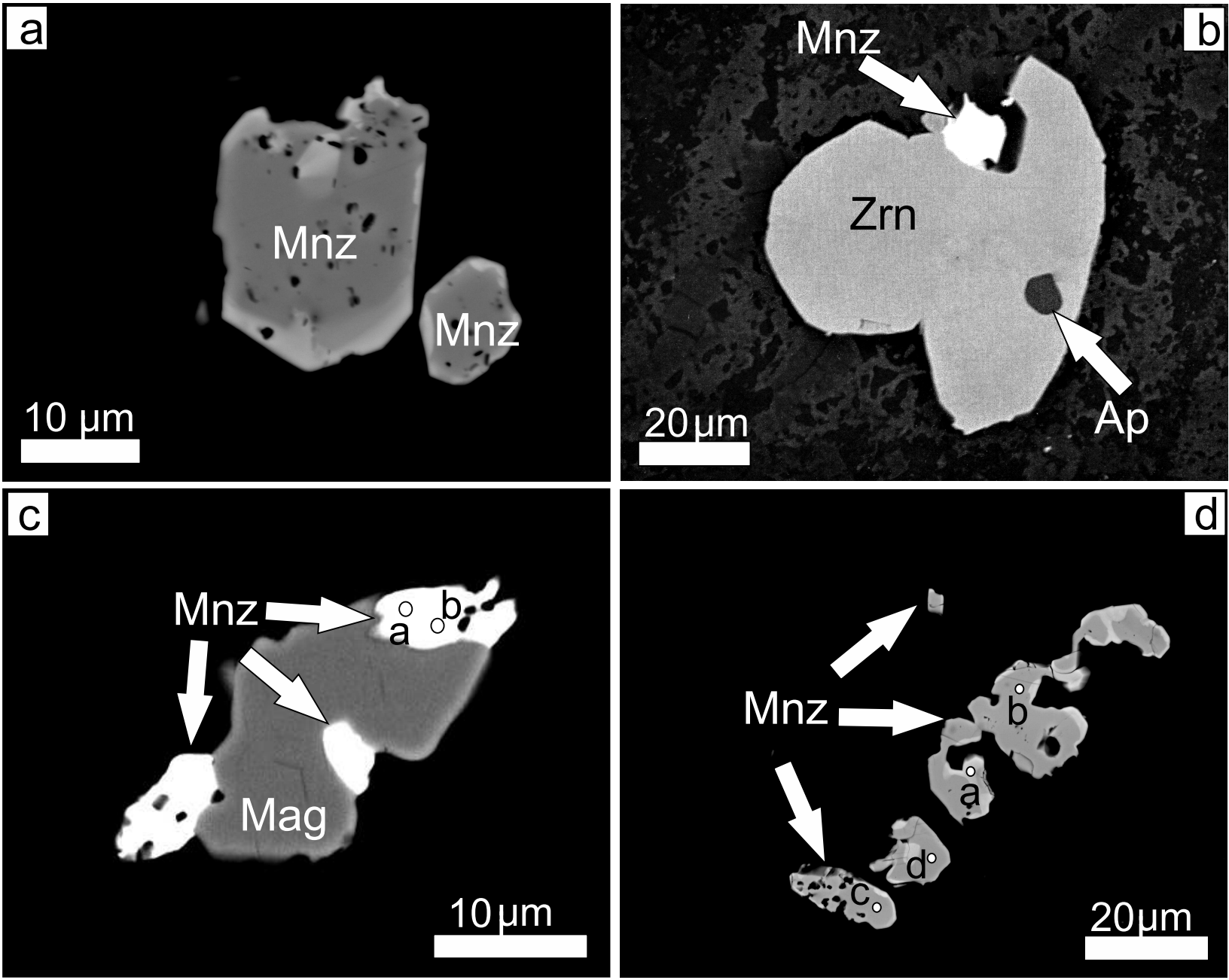

Figure 6

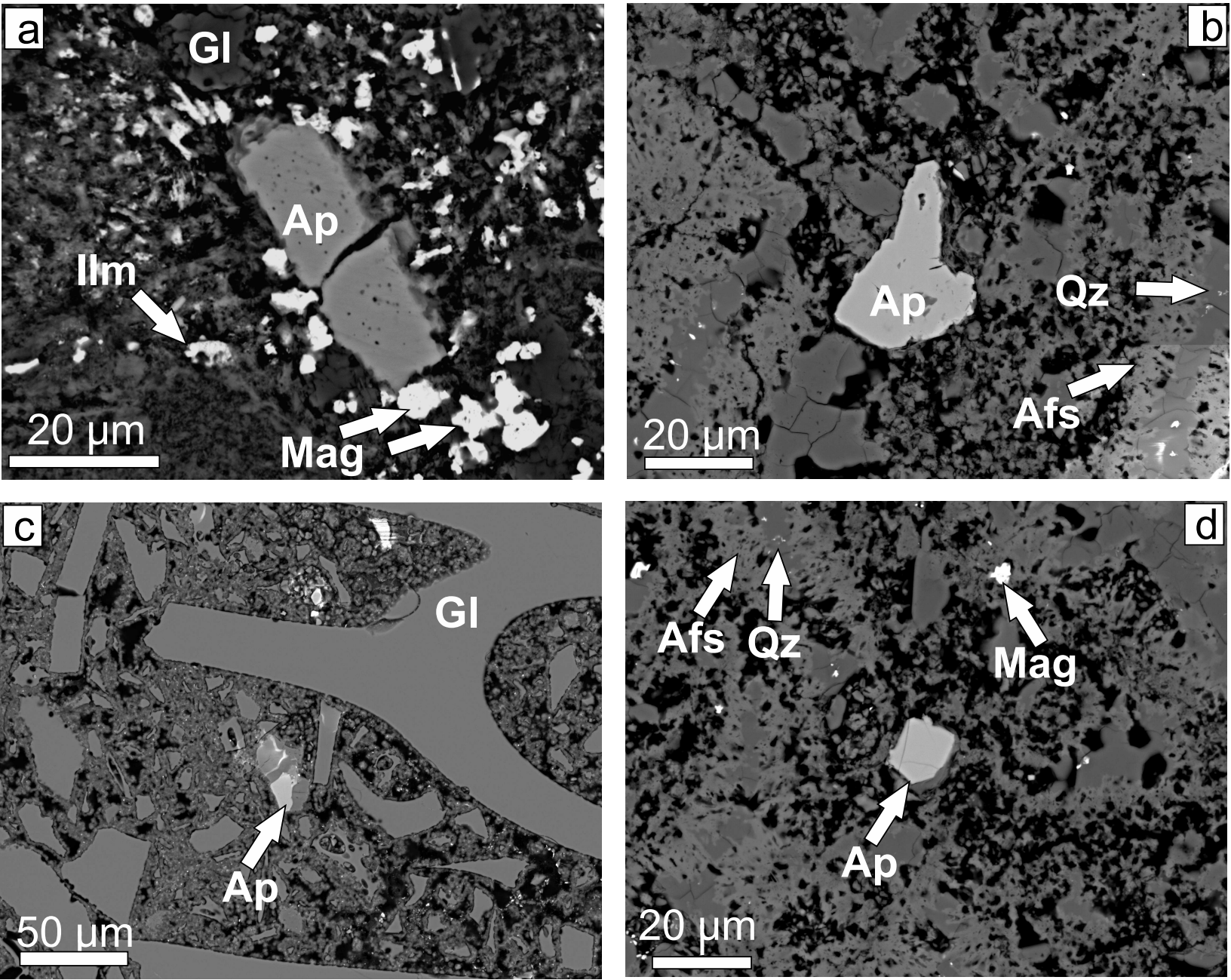
a
Gl
Ap
Ilm
Mag
20 µm
b
Ap
Qz
Afs
20 µm
c
Gl
Ap
50 µm
d
Afs
Qz
Mag
Ap
20 µm

Figure 7

Figure 8

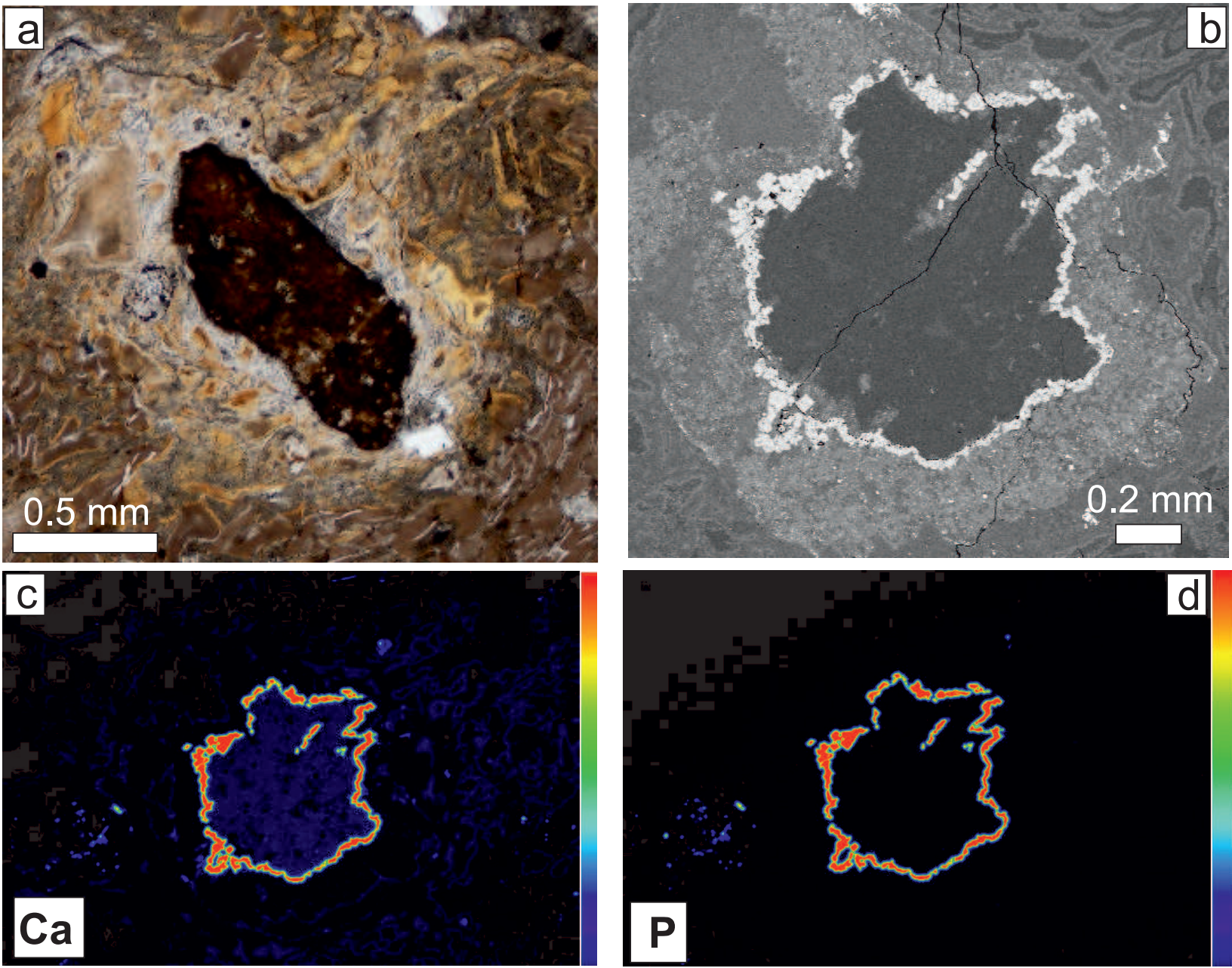

Figure 9

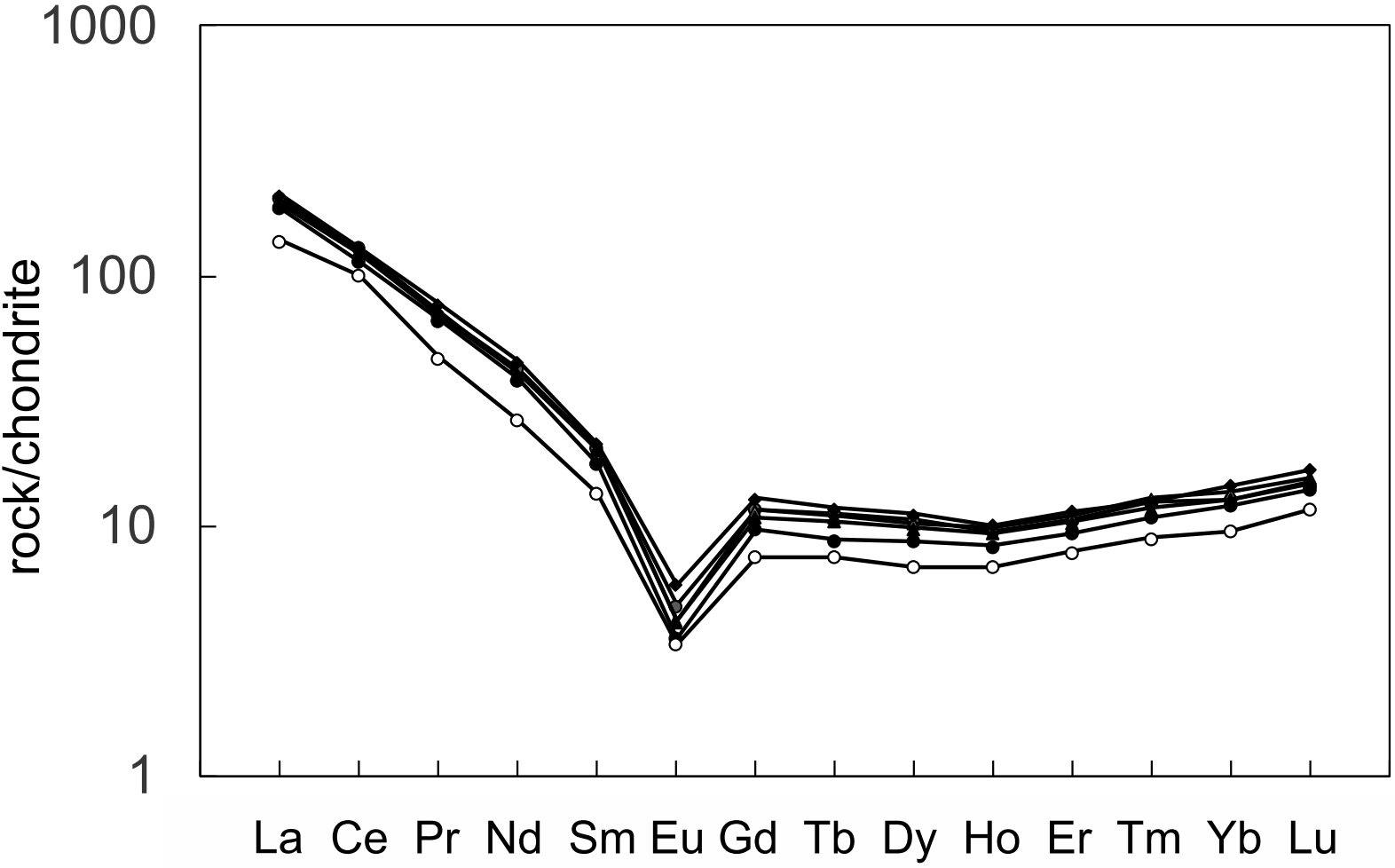
1000
100
10
1
rock/chondrite
La
Ce
Pr
Nd
Sm
Eu
Gd
Tb
Dy
Ho
Er
Tm
Yb
Lu

Figure 10

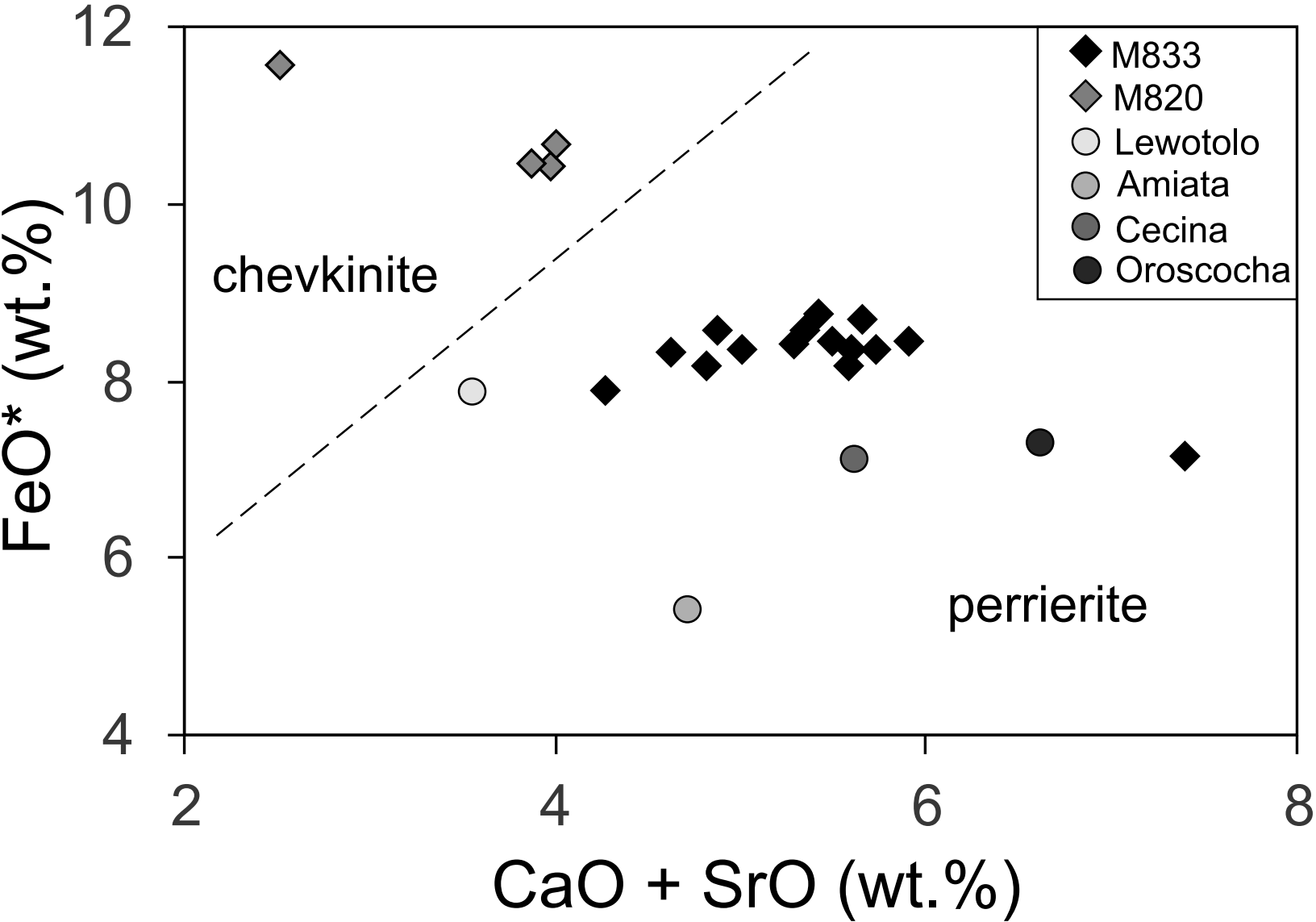
12
10
8
6
4
2
4
6
8
FeO* (wt.%)
CaO + SrO (wt.%)
chevkinite
perrierite
M833
M820
Lewotolo
Amiata
Cecina
Oroscocha

Figure 11

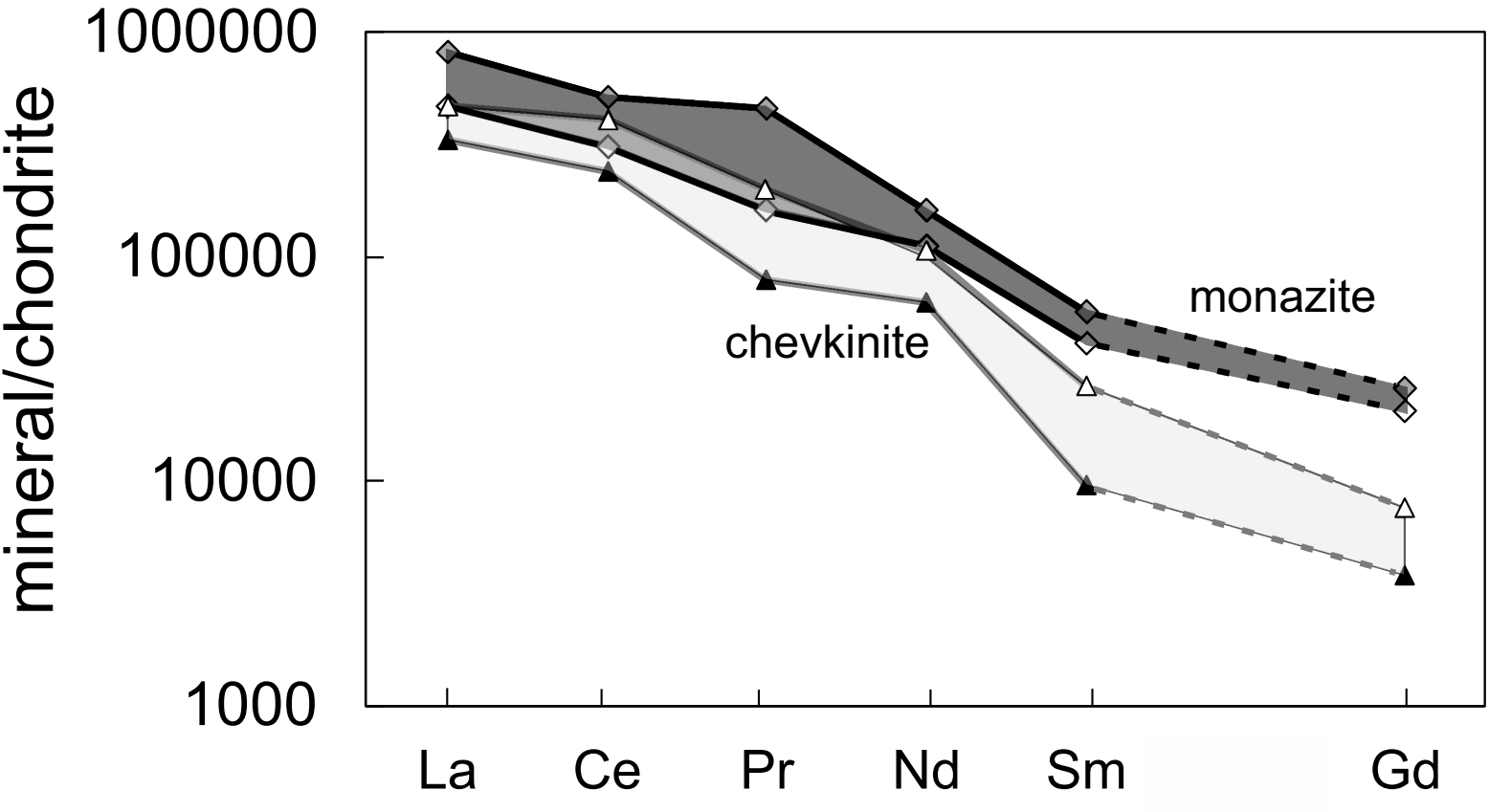
1000000
100000
10000
1000
mineral/chondrite
monazite
chevkinite
La
Ce
Pr
Nd
Sm
Gd

Figure 12

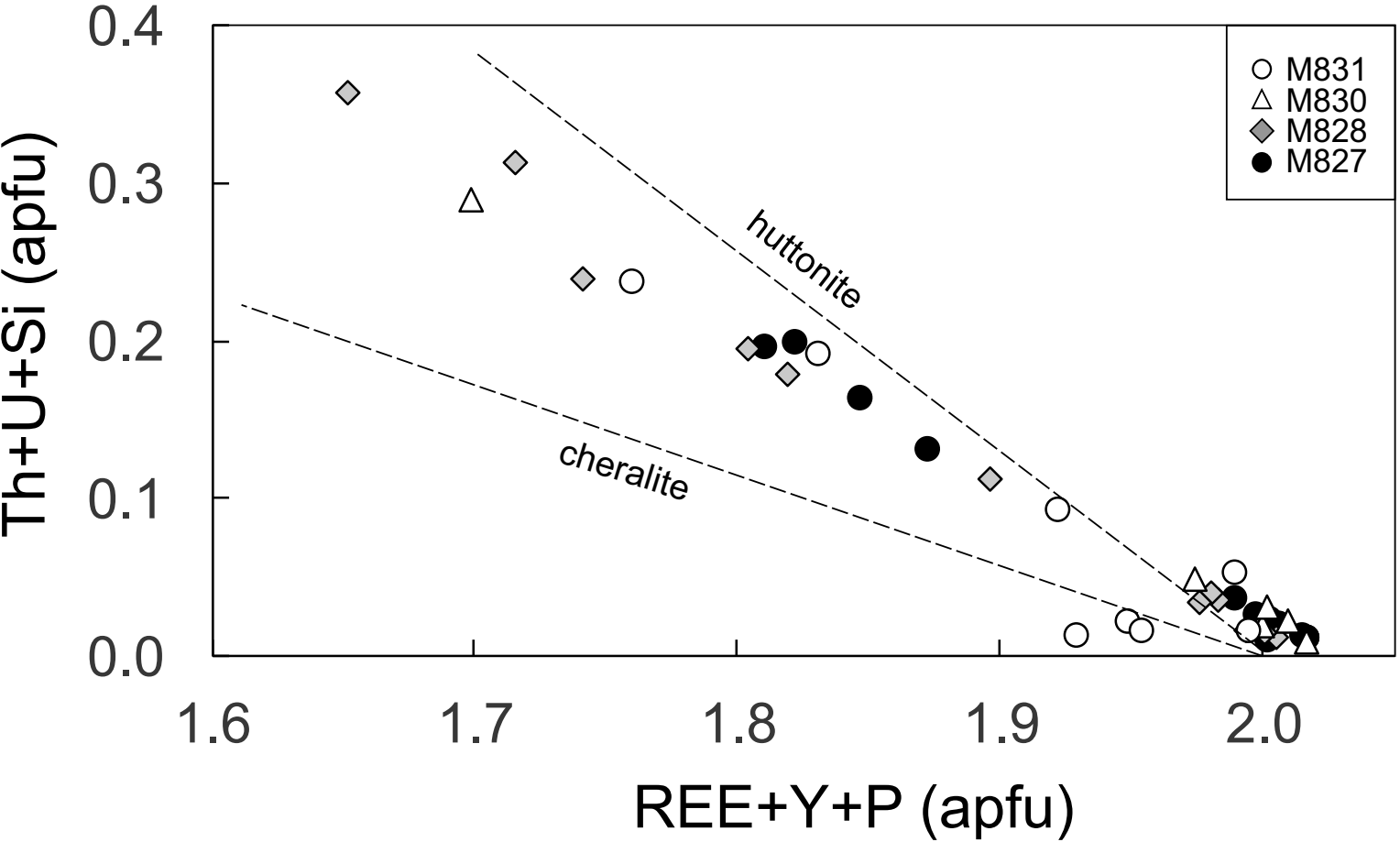
0.4
0.3
0.2
0.1
0.0
Th+U+Si (apfu)
1.6
1.7
1.8
1.9
2.0
REE+Y+P (apfu)
huttonite
cheralite
M831
M830
M828
M827

Figure 13

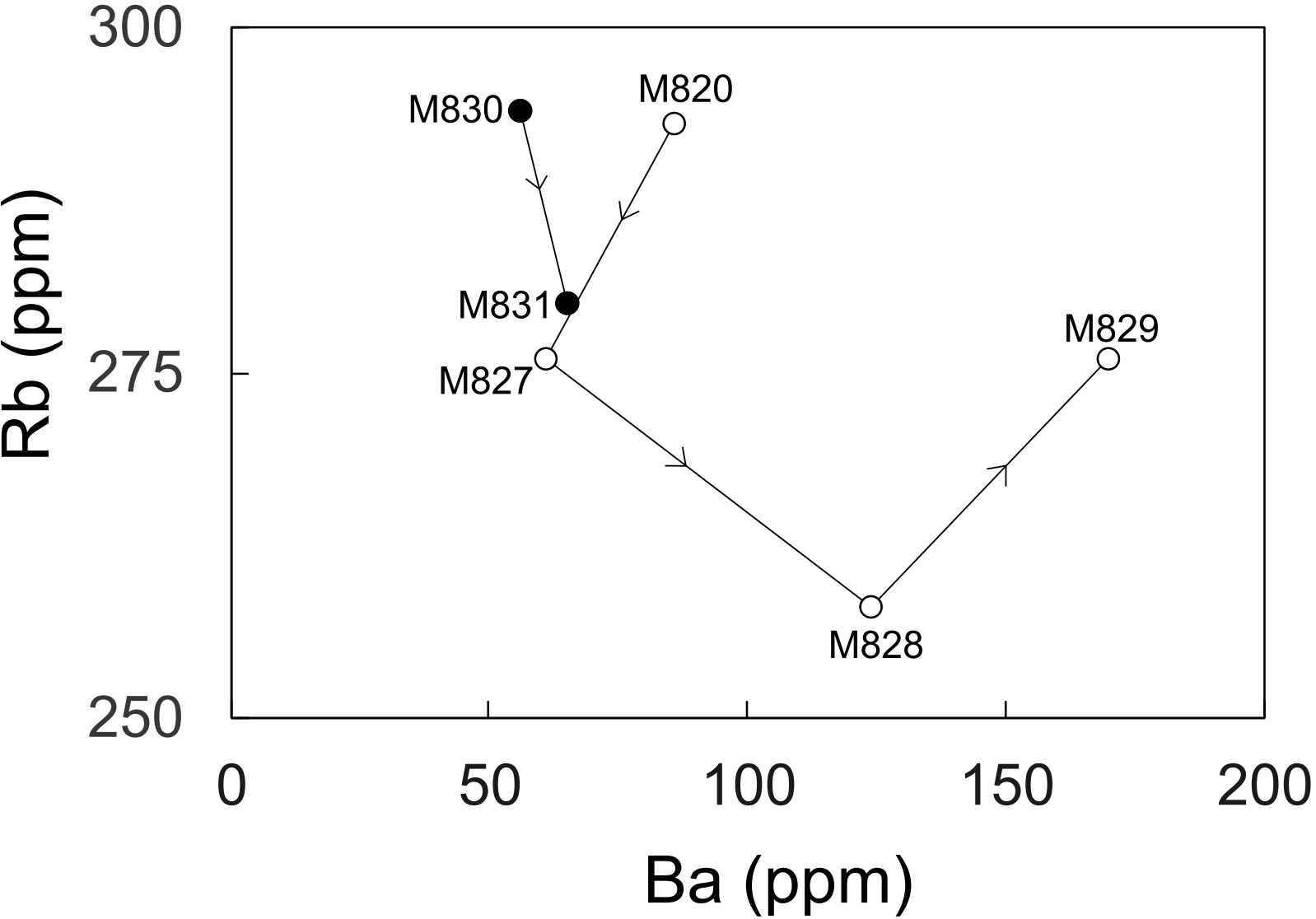
300
275
250
Rb (ppm)
M830
M820
M831
M827
M829
M828
0
50
100
150
200
Ba (ppm)

Figure 14

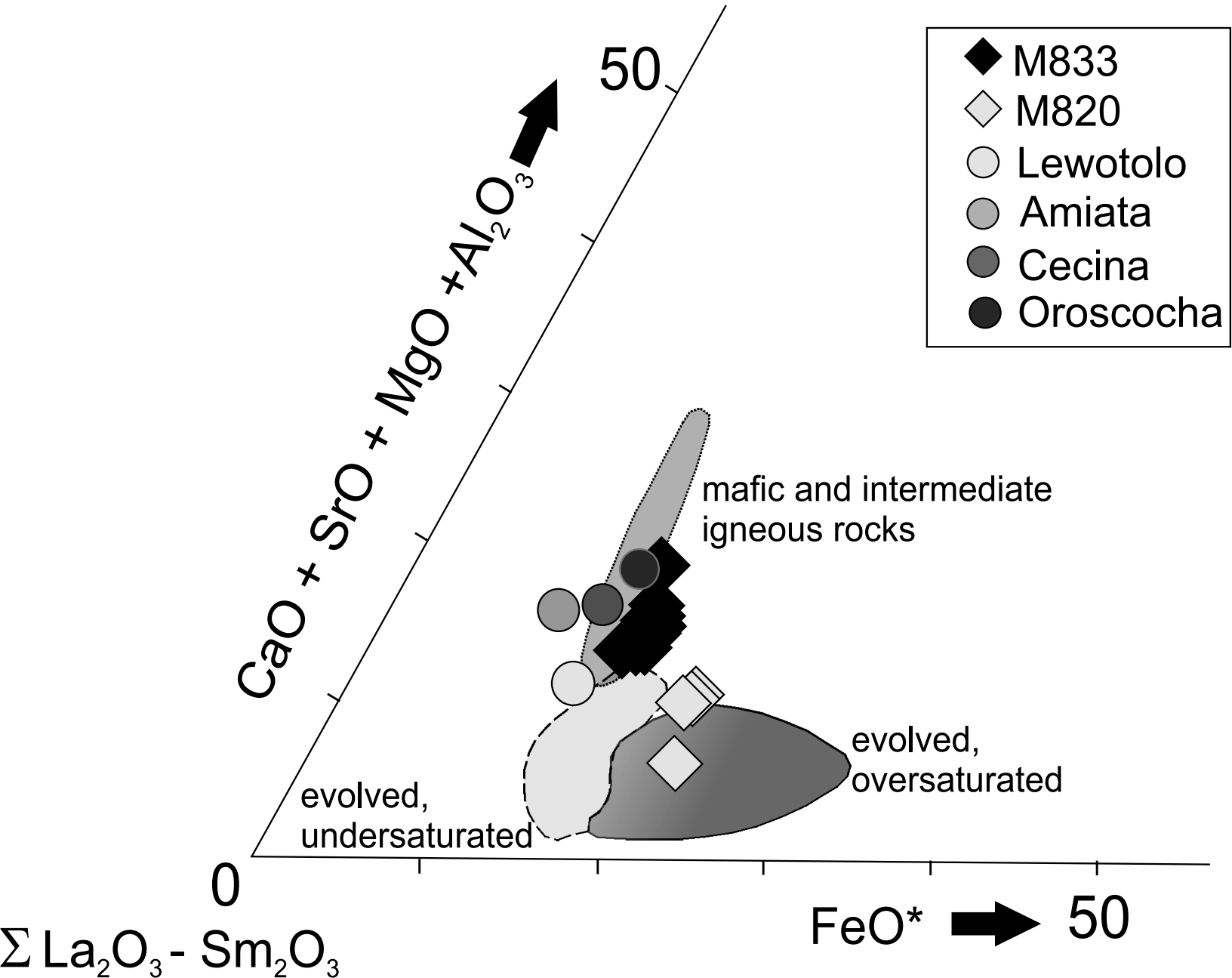
M833
M820
Lewotolo
Amiata
Cecina
Oroscocha
50
CaO + SrO + MgO +Al2O3
mafic and intermediate
igneous rocks
evolved,
oversaturated
evolved,
undersaturated
0
FeO*
50
Σ La2O3 - Sm2O3

Table 1

Click here to download Table: Joe Lott - Table 1 - phenocrysts.doc

Table 1. Phenocryst assemblages in Joe Lott Tuff

Unit Sample	Quartz	Alkali feldspar	Plagioclase	Augite	Biotite	FeTi-oxides	Zircon	Apatite	CGM	Monazite
Upper										
M833	+	+	+	+	+	+	+	+	+	-
Pink										
M832	+	+	+	+	+	+	+	+	-	-
Middle										
M831	+	+	+	+	-	+	+	+	-	+
M830	-	+	+	+	+	+	+	+	-	+
Lower										
M829	+	+	+	+	+	+	+	+	-	+
M828	+	+	+	+	+	+	+	+	-	+
M827	-	+	+	+	+	+	+	+	-	+
M820		+	+	+	+	+	+	+	+	-

Compiled from data in Budding et al. (1987) and this paper. CGM, chevkinite-group minerals.

Table 2

Click here to download Table: Joe Lott - Table 2 - w-r analyses.xls

Table 2

Whole-rock compositions of Joe Lott Tuff

Cooling unit	Lower Unit				Middle Unit		Pink Unit	Upper Unit
Sample	M820	M827	M828	M829	M830	M831	M832	M833
wt%								
SiO_2	73.30	74.60	71.30	73.80	74.50	74.52	71.62	74.18
TiO_2	0.15	0.12	0.13	0.13	0.13	0.13	0.15	0.13
Al_2O_3	12.60	12.30	12.20	13.00	13.10	12.66	12.85	13.12
FeO*	0.98	0.79	0.82	0.83	0.85	0.91	0.96	0.91
MnO	0.08	0.06	0.06	0.02	0.06	0.08	0.09	0.06
MgO	0.18	0.124	0.22	0.26	0.16	0.14	0.50	0.12
CaO	0.79	0.49	0.91	0.46	0.35	0.35	0.68	0.35
Na_2O	3.54	3.74	3.60	2.96	3.53	3.67	3.40	4.29
K_2O	4.59	5.01	4.80	5.22	5.36	5.05	3.69	5.21
P_2O_5	0.01	<0.01	0.02	0.01	<0.01	<0.01	0.01	0.02
LOI	4.20	2.25	4.72	3.11	1.55	0.94	5.57	1.32
Total	100.42	99.48	98.78	99.80	99.59	98.45	99.52	99.72
A/CNK	1.1	1.0	1.1	1.2	1.1	1.1	1.2	1.0
mg#	25	22	32	36	25	22	48	19
ppm								
Be	7	7	8	6	7	8	8	6
V	9	<5	5	13	6	5	7	8
Ni	2	<1	2	2	1	2	2	4
Cu	8	4	4	6	2	4	2	3
Zn	68	44	39	43	52	63	195	41
Ga	21	21	20	22	22	22	22	22
Ge	1.6	1.5	1.4	1.4	1.6	1.7	1.5	1.3
Mo	5	<2	<2	<2	<2	<2	5	<2
Ag	0.3	0.3	0.4	0.4	0.4	0.4	0.4	0.6
Sn	3	2	2	6	2	2	4	3
Rb	293	276	258	294	294	280	267	267
Sr	52	50	152	114	114	27	47	34
Cs	17.2	4.0	3.3	1.6	4.0	3.6	11	2.6
Ba	86	61	124	170	56	65	77	193
Sc	2	2	2	1	2	2	2	2
Y	18.2	15.1	16.1	14.2	20.1	17.2	20.6	18.1
La	49.2	44.3	44.2	32.9	47.9	46.6	49.9	45.8
Ce	79.7	70.2	71.2	61.7	77.2	76.3	79.8	74.6
Pr	6.70	6.31	6.30	4.49	6.82	6.76	7.36	6.65
Nd	20.0	18.0	17.4	12.4	19.0	19.2	21.2	19.1
Sm	3.14	2.71	2.76	2.07	3.08	2.78	3.27	3.12
Eu	0.28	0.21	0.22	0.20	0.24	0.24	0.34	0.24
Gd	2.40	1.99	2.06	1.55	2.37	2.26	2.66	2.22
Tb	0.42	0.33	0.35	0.28	0.41	0.39	0.44	0.39

Table 3

Click here to download Table: Joe Lott - Table 3 -glass - revision.xlsx

Table 3. Representative compositions of glass

Set	1	1	1	2	2	2	3	3
Sample	M820B	M820A	M820A	M820	M820B	M820B	M820A	M820A
Point	7/1.	15.0	19.0	1 / 1 .	9 / 1 .	18 / 1 .	1 / 1 .	2 / 1 .
wt%								
SiO_2	73.44	75.46	75.75	75.66	75.27	75.13	74.67	75.43
TiO_2	0.15	0.15	0.08	0.11	0.12	0.11	0.15	0.13
Al_2O_3	12.05	12.12	12.21	12.30	11.96	12.06	12.09	12.27
FeO*	1.91	0.80	0.19	0.10	0.12	0.43	0.76	0.24
MnO	0.13	0.10	bd	bd	bd	bd	0.08	bd
MgO	0.11	0.04	0.06	bd	bd	bd	0.05	bd
CaO	0.29	0.33	0.20	0.27	0.25	0.21	0.40	0.25
Na_2O	4.12	2.35	4.26	3.72	4.44	4.23	4.22	3.58
K_2O	4.94	4.94	5.06	4.95	4.97	5.10	5.03	5.07
F	0.31	bd	bd	bd	bd	bd	0.36	bd
Cl	0.11	0.11	0.06	0.11	0.11	0.08	0.12	0.11
SO_2	0.06	bd	bd	bd	bd	bd	bd	bd
Sum	97.62	96.40	97.87	97.22	97.25	97.36	97.92	97.07
O ≡ F, Cl	0.16	0.03	0.01	0.03	0.02	0.02	0.18	0.02
Total	97.46	96.37	97.86	97.19	97.23	97.35	97.74	97.05
A/CNK	0.97	1.27	0.96	1.05	0.93	0.95	0.95	1.06

FeO*, all Fe as Fe^{2+}. bd, below detection.

Details of glass types ar given in Supplementary Table 1.

Table 4

Click here to download Table: Joe Lott - Table 4 - CGM anals.xls

Table 4. Representative compositions of chevkinite-group minerals in Joe Lott Tuff

Sample	M820			M833				
	1	2	3	4	5	6	7	8
Host	quartz		glass	quartz		glass	alkali feldspar phen	
Form	euhedral		suhedral	oval, anhedral		elongate	elongate, subhedr	
Max.size	20 µm		20 µm	8 µm		55 µm	30 µm	
Species	C	C	C	P	P	P	P	P
wt.%								
Nb_2O_5	0.63	0.70	5.00	0.18	0.75	0.82	0.33	0.09
Ta_2O_5	0.08	0.16	0.49	0.12	0.13	0.08	bd	0.10
SiO_2	19.64	19.78	19.44	20.63	20.80	20.87	21.00	20.42
TiO_2	16.60	16.74	11.24	18.29	16.81	16.31	18.18	17.85
ZrO_2	0.48	0.44	0.26	1.11	0.61	0.81	0.87	0.67
HfO_2	0.09	bd	bd	0.20	0.17	0.09	0.09	0.09
ThO_2	7.15	5.93	3.13	1.70	1.58	1.90	1.91	1.37
UO_2	0.49	0.50	0.19	bd	bd	bd	bd	bd
Al_2O_3	0.78	0.75	0.63	2.07	1.91	2.04	2.15	2.03
Sc_2O_3	0.07	0.10	0.39	0.23	0.66	0.61	0.32	0.24
V_2O_3	0.24	0.16	bd	bd	bd	bd	bd	bd
Y_2O_3	0.58	0.50	0.55	0.39	0.69	0.72	0.30	0.32
La_2O_3	8.26	8.98	9.39	12.53	10.38	10.25	12.66	13.10
Ce_2O_3	18.40	18.74	21.88	19.58	20.41	20.41	19.43	19.96
Pr_2O_3	1.52	1.54	1.77	1.09	1.20	1.42	1.06	1.03
Nd_2O_3	5.99	6.12	5.23	3.62	4.90	4.39	3.69	3.64
Sm_2O_3	0.67	0.73	0.61	bd	0.45	0.37	0.43	0.35
Gd_2O_3	0.49	0.41	0.38	0.26	0.39	0.31	bd	bd
Dy_2O_3	0.17	0.29	bd	bd	bd	0.19	bd	bd
MgO	0.81	0.72	0.26	0.59	0.42	0.41	0.69	0.74
CaO	3.87	4.00	2.52	5.50	4.87	4.82	5.58	5.01
MnO	bd	bd	1.64	0.57	1.04	1.05	0.45	0.51
FeO*	10.46	10.67	11.57	8.46	8.56	8.18	8.17	8.37
Total	97.47	97.96	96.57	97.12	96.73	96.05	97.31	95.89
Formulae on the basis of 22 oxygens								
Ca	0.871	0.894	0.586	1.179	1.057	1.053	1.189	1.092
Th	0.342	0.282	0.155	0.077	0.073	0.088	0.086	0.063
U	0.023	0.023	0.009	0.000	0.000	0.000	0.000	0.000
Y	0.065	0.056	0.064	0.042	0.074	0.078	0.032	0.035
La	0.640	0.691	0.752	0.925	0.776	0.771	0.928	0.983
Ce	1.415	1.432	1.740	1.434	1.514	1.523	1.414	1.487
Pr	0.116	0.117	0.140	0.079	0.089	0.105	0.077	0.076
Nd	0.449	0.456	0.406	0.259	0.355	0.320	0.262	0.264
Sm	0.048	0.052	0.046	0.000	0.031	0.026	0.029	0.025
Gd	0.034	0.028	0.027	0.017	0.026	0.021	0.000	0.000

Table 5

Click here to download Table: Joe Lott - Table 5 - monazite.xls

Table 5. Representative compositions of monazite

Sample	M827			M828			M830	
	1	2	3	4	5	6	7	8
wt%								
P_2O_5	30.11	27.10	25.89	25.62	29.36	22.87	24.18	29.10
Nb_2O_5	-	-	-	-	bd	bd	0.04	bd
Ta_2O_5	-	-	-	-	bd	bd	bd	bd
SiO_2	0.23	1.77	2.54	3.22	0.20	4.59	4.29	0.19
TiO_2	-	-	-	-	bd	bd	bd	bd
ZrO_2	-	-	-	-	0.10	0.04	0.07	0.07
HfO_2	-	-	-	-	bd	bd	bd	bd
ThO_2	0.13	6.25	9.81	11.28	0.40	16.97	12.12	0.09
UO_2	0.10	0.13	0.15	0.09	0.08	0.17	0.18	0.11
Al_2O_3	bd	bd	bd	0.11	bd	0.09	0.23	bd
Sc_2O_3	-	-	-	-	bd	bd	0.01	bd
V_2O_3	-	-	-	-	bd	bd	0.34	bd
Cr_2O_3	-	-	-	-	bd	bd	0.06	0.06
As_2O_3	bd	bd	bd	0.04	0.06	0.09	0.09	bd
Y_2O_3	0.22	0.17	0.06	0.64	0.60	0.32	0.31	0.46
La_2O_3	20.16	18.51	17.21	13.20	18.49	14.30	18.18	21.09
Ce_2O_3	36.01	32.90	31.75	26.43	36.17	28.00	28.07	36.11
Pr_2O_3	3.68	3.21	3.08	2.88	3.41	2.66	2.82	3.17
Nd_2O_3	8.14	7.10	7.47	10.26	8.93	7.60	7.13	7.35
Sm_2O_3	0.62	0.61	0.43	1.58	1.10	0.89	0.74	0.86
Gd_2O_3	0.26	0.21	bd	0.85	0.67	0.52	0.52	0.43
Dy_2O_3	bd	bd	bd	0.12	bd	bd	bd	0.10
Tb_2O_3	0.21	bd	bd	bd	-	-	-	-
Lu_2O_3	bd	bd	bd	bd	bd	0.04	0.02	bd
MgO	bd	bd	bd	bd	bd	0.10	0.04	bd
CaO	0.74	0.13	0.08	0.33	0.19	0.16	0.14	0.37
MnO	bd	bd	bd	0.06	bd	bd	bd	bd
FeO*	bd	1.07	0.20	0.64	0.35	0.07	0.83	0.19
SrO	bd	bd	bd	bd	bd	bd	bd	bd
BaO	-	-	-	-	bd	0.07	0.08	bd
PbO	bd	bd	bd	0.02	bd	bd	bd	bd
Na_2O	-	-	-	-	bd	bd	bd	bd
K_2O	-	-	-	-	0.02	0.10	0.09	0.02
SO_2	bd	0.09	bd	0.05	0.04	0.05	0.10	bd
Cl	-	-	-	-	0.02	0.03	0.03	0.02
Total	100.63	99.25	98.68	97.41	100.20	99.74	100.73	99.79

Table 6

Click here to download Table: Joe Lott - Table 6 - apatite.xls

Table 6

Representative compositions of apatite and fluorapatite in Joe Lott Tuff

Sample	M827		M828	M829		M831	M832	M83
	ap1-1	ap1-4	ap-5	ap2-2	ap-3	ap-2	ap-1	ap2-1
wt%								
P_2O_5	40.94	39.32	39.79	39.57	37.86	41.45	40.69	41.43
SiO_2	bd	bd	0.80	0.78	2.86	0.53	0.25	0.26
ThO_2	bd	bd	bd	bd	bd	bd	bd	bd
UO_2	bd	bd	bd	bd	bd	bd	bd	bd
Al_2O_3	bd	bd	0.23	bd	0.23	0.24	0.05	0.12
Y_2O_3	bd	bd	0.09	bd	bd	0.14	bd	bd
La_2O_3	0.19	0.24	bd	0.23	0.11	bd	0.15	bd
Ce_2O_3	0.35	0.45	bd	0.16	0.23	0.15	0.18	0.21
Pr_2O_3	bd	bd	bd	bd	bd	bd	bd	bd
Nd_2O_3	bd	0.23	bd	bd	bd	bd	bd	bd
Dy_2O_3	0.26	0.30	bd	bd	bd	bd	bd	bd
MgO	bd	bd	0.04	0.04	0.06	0.06	bd	bd
CaO	54.66	55.29	53.82	55.12	51.52	55.41	52.93	55.09
MnO	bd	bd	0.37	bd	0.10	bd	bd	0.29
FeO*	bd	bd	0.11	bd	bd	bd	0.11	bd
SrO	bd	bd	bd	1.08	bd	bd	bd	bd
Na_2O	bd	bd	0.08	bd	0.16	0.10	bd	0.18
K_2O	bd	bd	-	-	-	-	0.05	0.11
F	bd	bd	2.23	1.33	1.66	1.88	1.87	2.55
Cl	0.07	0.15	bd	bd	0.74	0.97	0.15	0.22
Sum	96.46	95.98	97.55	98.31	95.53	100.93	96.41	100.45
O ≡ F, Cl	0.02	0.05	0.94	0.57	0.87	1.01	0.82	1.12
Total	96.44	96.02	96.60	97.74	94.67	99.92	95.59	99.33
Formulae on the basis of 13 oxygens								
Na	0.000	0.000	0.013	0.000	0.028	0.017	0.000	0.030
K	0.000	0.000	0.000	0.000	0.000	0.000	0.005	0.012
Mg	0.000	0.000	0.005	0.006	0.008	0.007	0.000	0.000
Ca	5.226	5.366	5.065	5.211	4.942	5.053	5.024	5.041
Mn	0.000	0.000	0.028	0.000	0.008	0.000	0.000	0.021
Fe	0.000	0.000	0.008	0.000	0.000	0.000	0.008	0.000
Sr	0.000	0.000	0.000	0.055	0.000	0.000	0.000	0.000
Al	0.000	0.000	0.024	0.000	0.024	0.024	0.005	0.012
Y	0.000	0.000	0.004	0.000	0.000	0.006	0.000	0.000
La	0.006	0.008	0.000	0.007	0.004	0.000	0.005	0.000
Ce	0.011	0.015	0.000	0.005	0.008	0.005	0.006	0.006
Pr	0.000	0.000	0.000	0.000	0.000	0.000	0.000	0.000
Nd	0.000	0.007	0.000	0.000	0.000	0.000	0.000	0.000
Dy	0.008	0.009	0.000	0.000	0.000	0.000	0.000	0.000
Th	0.000	0.000	0.000	0.000	0.000	0.000	0.000	0.000
U	0.000	0.000	0.000	0.000	0.000	0.000	0.000	0.000

Supplementary Table 1
Click here to download Table: Joe Lott - ST 1 - glass anals.xlsx

Supplementary Table 1. Compositions of matrix glass in basal vitrophyre

Set 1

Sample	M820B							
Occurrence	large grey fiamma				large grey fiamma			white fiamm
Point	1	2	3	4	5	6	7	8
SiO_2	75.77	75.15	75.26	75.18	74.55	75.33	73.44	74.49
TiO_2	0.10	0.10	0.12	0.08	0.09	0.08	0.15	0.12
Al_2O_3	12.32	12.16	12.12	11.79	11.78	11.96	12.05	12.06
FeO*	0.17	0.28	0.13	0.48	0.54	0.51	1.91	0.83
MnO	bd	bd	bd	bd	bd	bd	0.13	0.07
MgO	bd	bd	0.02	bd	bd	bd	0.11	0.10
CaO	0.26	0.25	0.26	0.45	0.39	0.44	0.29	0.27
Na_2O	4.24	4.14	4.23	4.13	4.05	3.95	4.12	4.17
K_2O	4.99	5.12	4.93	4.72	4.90	4.87	4.94	5.01
F	bd	bd	0.28	bd	0.33	0.32	0.31	0.32
Cl	0.12	0.10	0.12	0.04	0.05	0.05	0.11	0.09
SO_2	bd	bd	bd	bd	bd	bd	0.06	0.08
Total	97.96	97.38	97.47	96.88	96.66	97.51	97.62	97.62
A/CNK	0.98	0.97	0.97	0.96	0.96	0.98	0.97	0.96

Set 2

Sample	M820B							
Occurrence							large grey fiamma	
Point	1	2	3	4	5	6	7	8
SiO_2	75.66	75.09	75.28	75.22	75.23	74.82	74.61	74.90
TiO_2	0.11	0.14	0.12	0.14	0.12	0.12	0.11	0.11
Al_2O_3	12.30	12.19	12.11	12.11	11.93	11.86	12.07	12.08
FeO*	0.10	0.11	0.12	0.09	0.14	0.22	0.64	0.31
MnO	bd	bd	0.06	0.07	bd	bd	bd	bd
MgO	bd	bd	bd	bd	bd	bd	0.05	0.03
CaO	0.27	0.26	0.26	0.29	0.27	0.30	0.27	0.30
Na_2O	3.72	4.13	4.18	4.10	4.10	3.94	4.11	4.18
K_2O	4.95	5.04	5.08	4.97	5.05	5.18	5.20	5.15
CaO	0.27	0.26	0.26	0.29	0.27	0.30	0.27	0.30
F	bd	bd	bd	bd	bd	bd	bd	bd
Cl	0.11	0.11	0.10	0.11	0.12	0.11	0.12	0.13
SO_2	bd	0.05	bd	bd	bd	0.05	0.04	bd
Sum	97.22	97.12	97.30	97.11	96.95	96.62	97.22	97.18
O ≡ F, Cl	0.03	0.02	0.02	0.03	0.03	0.03	0.03	0.03
Total	97.19	97.09	97.28	97.08	96.93	96.59	97.19	97.15
A/CNK	1.05	0.98	0.96	0.98	0.96	0.96	0.96	0.95

Supplementary Table 2

Click here to download Table: Joe Lott - ST2 - CGM, monaz., apatite.xls

Supplementary Table 2a.

Compositions of chevkinite-group minerals in Joe Lott Tuff

Sample	M820				M833			
	1	2	3	4	5	6	7	8
Host	quartz			glass	quartz			quartz
Form	euhedral crystal			subhedral	euhedral, zoned			anhedral
Size	21 x 18 µm			16x11 µm	16 x 15 µm			7 x 5 µm
Species	C	C	C	C	P	P	P	P
wt%								
Nb_2O_5	0.74	0.63	0.70	5.00	0.18	0.77	0.75	0.16
Ta_2O_5	0.12	0.08	0.16	0.49	0.12	0.12	0.13	0.08
SiO_2	19.76	19.64	19.78	19.44	20.63	20.53	20.80	20.75
TiO_2	16.91	16.60	16.74	11.24	18.29	16.70	16.81	18.13
ZrO_2	0.48	0.48	0.44	0.26	1.11	0.52	0.61	0.91
HfO_2	bd	0.09	bd	bd	0.20	0.14	0.17	0.13
ThO_2	5.62	7.15	5.93	3.13	1.70	2.05	1.58	1.68
UO_2	0.53	0.49	0.50	0.19	bd	bd	bd	bd
Al_2O_3	0.72	0.78	0.75	0.63	2.07	2.13	1.91	1.87
Sc_2O_3	0.08	0.07	0.10	0.39	0.23	0.62	0.66	0.21
V_2O_3	0.27	0.24	0.16	0.05	bd	bd	bd	bd
Y_2O_3	0.50	0.58	0.50	0.55	0.39	0.69	0.69	0.39
La_2O_3	9.10	8.26	8.98	9.39	12.53	10.26	10.38	11.96
Ce_2O_3	19.30	18.40	18.74	21.88	19.58	20.66	20.41	18.96
Pr_2O_3	1.67	1.52	1.54	1.77	1.09	1.51	1.20	1.16
Nd_2O_3	5.41	5.99	6.12	5.23	3.62	4.96	4.90	3.55
Sm_2O_3	0.60	0.67	0.73	0.61	bd	0.32	0.45	0.38
Gd_2O_3	0.21	0.49	0.41	0.38	0.26	0.26	0.39	0.23
Dy_2O_3	bd	bd	0.29	bd	bd	bd	bd	bd
MgO	0.69	0.81	0.72	0.26	0.59	0.46	0.42	0.58
CaO	3.98	3.87	4.00	2.52	5.50	4.63	4.87	5.73
MnO	bd	bd	bd	1.64	0.57	1.14	1.04	0.58
FeO*	10.42	10.46	10.67	11.57	8.46	8.32	8.56	8.37
Total	97.11	97.3	97.96	96.62	97.12	96.79	96.73	95.81
Formulae on basis of 22 oxygens								
Ca	0.892	0.871	0.894	0.586	1.179	1.009	1.057	1.239
Th	0.268	0.342	0.282	0.155	0.077	0.095	0.073	0.077
U	0.025	0.023	0.023	0.009	0.000	0.000	0.000	0.000
Y	0.056	0.065	0.056	0.064	0.042	0.075	0.074	0.042
La	0.703	0.640	0.691	0.752	0.925	0.770	0.776	0.890
Ce	1.479	1.415	1.432	1.740	1.434	1.539	1.514	1.401
Pr	0.127	0.116	0.117	0.140	0.079	0.112	0.089	0.085
Nd	0.404	0.449	0.456	0.406	0.259	0.360	0.355	0.256
Sm	0.043	0.048	0.052	0.046	0.000	0.022	0.031	0.026

Supplementary Material 1

Click here to download Table: Joe Lot - Supplementary Material 1.docx

Supplementary Material 1. Analytical conditions for chevkinite-(Ce)

Element	Line	Crystal	Standard	Approx. detection limit (ppm)
Al	Kα	TAP	orthoclase	200
Ca	Lα	PET	diopside	300
Ce	Kα	PET	$CePO_4$	900
Dy	Lß	LLIF	DyP_5O_{14}	1800
Fe	Kα	LIF	hematite	800
Gd	Lß	LLIF	GdP_5O_{14}	1900
Hf	Mα	TAP	HfO_2	600
La	Lα	PET	La glass	900
Mg	Kα	TAP	diopside	200
Mn	Kα	LIF	rhodonite	900
Nb	Lα	PET	Nb metal	800
Nd	Lß	LIF	$NdGaO_3$	2200
Pr	Lß	LIF	Pr glass	1800
Sc	Kα	PET	Sc metal	300
Si	Kα	TAP	diopside	300
Sm	Lß	LLIF	SmP_5O_{14}	1800
Ta	Mα	TAP	Ta metal	700
Th	Mα	PET	ThO_2 synthetic	1200
Ti	Kα	PET	rutile	600
U	Mß	PET	vorlanite	1200
V	Kα	LIF	V_2O_5	800
Y	Lα	TAP	YPO_4	700
Zr	Lα	PET	zircon ED	800

Acceleration. voltage 15 kV, probe current 50 nA, L- large crystal

Supplementary Material 2

Click here to download Table: Joe Lott - Supplementary Material 2.xlsx

Supplementary Material 2. Analytical conditions for monazite on Cameca SXFiveFE microprobe

Element/ x-ray line	Diffracting Crystal	Peak overlap Correction	Standard	Approx. det. Limit (ppm)	Peak/backg. Time (s)
Al Kα	TAP		Al_2O_3	90 – 260	30/30
As Lα	TAP	Nd M_2N_4	GaAs	140 – 710	40/80
Ba Lα	TAP	Ti Kα	Barite	650 – 930	30/30
Ca Kα	LPET		Wollastonite	60 – 240	30/60
Ce Lα	LPET		$CePO_4$	200 – 620	30/30
Cl Kα	LPET	Nd Lα ^{2nd}	Sodalite	30 – 100	30/60
Cr Kα	LLIF		Cr_2O_3	250 – 360	30/60
Dy Lα	LLIF	Mn Kβ	$DyPO_4$	510 – 1660	30/60
Er Lα	LLIF	Tb Lβ_4, Fe Kβ	$ErPO_4$	290 – 1280	30/60
Eu Lα	LLIF	Pr Lβ_2, Nd Lβ_3, Mn Kα	$EuPO_4$	2 – (1680)	30/60
Fe Kα	LLIF		Hematite	230 – 460	20/40
Gd Lα	LLIF	La Lγ_2, Ce Lγ, Nd Lβ_2	$GdPO_4$	40 – 320	30/40
Hf Mα	TAP		HfO_2	(880)	30/60
K Kα	LPET		Orthoclase	90 – 130	30/20
Lα Lα	LPET	Nd Ll	$LaPO_4$	260 – 990	30/30
Lu Mα	LTAP	Yb Mβ	$LuPO_4$	120 – 170	100/200
Mg Kα	LTAP		MgO	70 – 380	30/60
Mn Kα	LLIF		Rhodonite	240 – 660	20/40
Na Kα	TAP		Sodalite	260 – 370	15/30
Nb Lα	LPET		Nb (metal)	300 – 440	30/60
Nd Lα	LLIF	Ce Lβ	$NdPO_4$	700 – 2050	30/30
P Kα	LPET	Y Lβ	$CePO_4$	150 – 580	30/60
Pb Mβ	LPET		Crocoite	120 – 600	50/80
Pr Lα	LPET	La Lβ, V Kα	$PrPO_4$	90 – 340	30/40
S Kα	LPET		FeS_2	60 – 180	30/30
Sc Kα	LPET		Sc (metal)	80 – 110	30/60
Si Kα	TAP	Nd Lα ^{3rd}	SiO_2	90 – 250	20/20
Sm Lα	LLIF	Ce Lβ_2	$SmPO_4$	410 – 1270	20/30
Sr Lα	LPET		$SrSO_4$	280 – 780	30/60
Ta Mα	TAP		LiTaO3	340 – 470	40/80
Tb Lα	LLIF		$TbPO_4$	480 – 1340	30/60
Th Mα	LPET		ThO_2	190 – 530	40/80
Ti Kα	LLIF	Hf Lβ ^{2nd}, U M_1N_3, Sc Kβ	TiO_2	90 – 130	30/40
U Mα	LPET	Th Mβ	UO_2	50 – 450	50/100
V Kα	LLIF	Ti Kα	V (metal)	250 – 340	30/60
Y Lα	TAP		YAG	140 – 420	40/40
Yb Mα	LTAP	Dy Mγ	$YbPO_4$	(780)	100/100
Zr Lα	LPET		Zr (metal)	230 – 320	60/120

Detection limits and standard deviation are given as ranges, as they are dependent on counting time and beam curren which in this experiment ranged from 20 to 150 nA per point basis.

The det. lim. approximation, which takes into account beam current and counting times, is reported by Cameca Peak

Supplementary Material 3

Click here to download Table: Joe Lott - Supplementary Material 3.xlsx

Supplementary Material 3. Analytical conditions for matrix glass on SXFiveFE EPMA

Element/ x-ray line	Crystal	Standard	Approx. Det. Limit (ppm)	Peak/Backg. Time (s)	Approx. Std Dev. wt%
Al Kα	TAP	Al_2O_3	170	30/40	0.12
Ca Kα	LPET	Wollastonite	160	20/40	0.02
Cl Kα *	LPET	Sodalite	260	15/30	0.03
F Kα *	LTAP	Topaz (synth.)	2700	15/30	0.26
Fe Kα	LLIF	Hematite	490	30/60	0.06
K Kα	LTAP	Orthoclase	230	20/20	0.20
Mg Kα	LTAP	MgO	130	20/40	0.01
Mn Kα	LLIF	Rhodonite	460	30/60	0.04
Na Kα *	TAP	Sodalite	490	15/30	0.19
P Kα	LPET	$CePO_4$	220	20/40	–
S Kα	LPET	FeS_2	200	20/20	0.02
Si Kα	TAP	SiO_2	220	20/40	0.44
Ti Kα	LPET	TiO_2	190	20/40	0.02
Zr Lα	LPET	Zr (metal)	1050	30/60	–

Approximate detection limits and standard deviations is given
for single points for given counting time and 10 nA beam current
* Cl, F and Na were measured first with "time 0 intercept" option

Supplementary Material 4

Click here to download Table: Joe Lott - Supplementary Material 4.docx

Supplementary Material 4. Analytical conditions for apatites

Element	*Line*	*Crystal*	*Standard*	*Approx. detection limit (ppm)*
Al	Kα	TAP	orthoclase	300
Ca	Kα	PET	diopside	450
Ce	Lα	PET	$CePO_4$	1000
Dy	Lß	LIF	$DyPO_4$	900
Cl	Lß	LLIF	tugtupite	300
F	Kα	TAP	apatite	9000
Fe	Kα	LIF	hematite	800
La	Lα	PET	$LaPO_4$	1000
K	Kα	PET	orthoclase	400
Mg	Kα	TAP	diopside	250
Mn	Kα	LIF	rhodonite	800
Na	Kα	TAP	albite	200
Nd	Lß	LLIF	$NdGaO_3$	1400
P	Kα	PET	apatite	600
Pr	Lß	LIF	Pr glass	2400
Si	Kα	TAP	diopside	200
Sr	Lα	TAP	celestine	700
Th	Mα	PET	ThO_2 synthetic	1600
U	Mß	PET	vorlanite	1800
Y	Lα	TAP	YPO_4	600

Acceleration voltage used - 15 kV, probe current - 20 nA, LLIF- large crystal

***Declaration of Interest Statement**

Statement of interest

We confirm that there were no financial relationships with other people or organizations that inappropriately influenced this work.